Revista Mexicana de Astronomía y Astrofísica, 62, 87-107, (2026)

OPEN ACCESS https://doi.org/10.22201/ia.30618649p.2026.62.01.08

SDSS-V Local Volume Mapper (LVM): Helix Nebula public data, Data Analysis Pipeline data products

S. F. Sánchez [1,2,†], J.E. Méndez-Delgado [3], A. Mejía-Narváez [4], C. Román-Zuñiga [1], O. V. Egorov [5], C. Morisset [6], N. Drory [7], G. A. Blanc [8,4], K. Kreckel [5], E. J. Johnston [9], Ivan Yu. Katkov [10,11,12], A. Roman Lopes [13], M. A. Villa-Durango [1], H. Ibarra-Medel [3], H.-W. Rix [14], R. de J. Zermeño [1], J. G. Fernández Trincado [15,16], A. Singh [4], P. García [17,18], G. S. Stringfellow [19], L. Sabin [1], J. Toalá [20], R. Orozco Duarte [20] and A. M. Jones [21]

[1] *Universidad Nacional Autónoma de México, Instituto de Astronomía, AP 106, Ensenada 22800, BC, México.*
[2] *Instituto de Astrofisica de Canarias, La Laguna, Tenerife, E-38200, Spain. The remaining affiliations are listed at the end of the paper.*

Keywords: *ISM: kinematics and dynamics, ISM: lines and bands, methods: data analysis, planetary nebulae: individual: NGC 7293, techniques: imaging spectroscopy*

Abstract

We present a spatially resolved spectroscopic analysis of the Helix Nebula (NGC 7293) using data from the SDSS-V Local Volume Mapper (LVM) by applying the recently developed LVM Data Analysis Pipeline (LVM-DAP). Covering the full optical range (3600-9800Å) over a contiguous $\sim 0.5°$ field, the LVM data provide the first hexagonally sampled wide-field emission line maps of all major ionic species in this archetypal planetary nebula. The resulting flux, kinematic, and line-ratio maps reveal the well-known ionization stratification of the nebula, from the compact He^{++} core to the bright [O III] ring and the extended low-ionization envelope, enabling a detailed comparison with the classical aperture spectroscopy. Owing to the sensitivity and uniform spatial sampling of the LVM, numerous faint auroral and diagnostic lines are detected across the nebula, including [O III] 4363, [N II] 5755, and He I lines, allowing for precise measurements of the weak-line morphology. The derived radial trends confirm the remarkably low dust content and overall homogeneity of the electron temperature and density across the main ring. Ionized-gas kinematics traced by Hα further support the scenario of a slowly expanding, limb-brightened shell, consistent with previous studies. This study demonstrates the diagnostic power of LVM spectroscopy for extended nebulae and highlights its capability to recover both global and spatially resolved physical conditions across complex ionized structures.

Resumen

Presentamos un análisis espectroscópico espacialmente resuelto de la Nebulosa de la Hélice (NGC 7293) con datos del SDSS-V Local Volume Mapper (LVM), procesados con el LVM Data Analysis Pipeline (LVM-DAP). Cubriendo 3600–9800 Å sobre un campo contiguo de $\sim 0.5°$, el LVM provee de los primeros mapas de líneas de emisión de campo amplio, muestreados hexagonalmente, de las principales especies iónicas en esta nebulosa planetaria arquetípica. Los mapas de flujo, cinemática y cocientes de líneas revelan la estratificación de ionización desde el núcleo compacto de He^{++} hasta el anillo brillante de [O III] y la envoltura extendida de baja ionización, permitiendo una comparación detallada con datos de espectroscopía clásica de apertura. Gracias a la sensibilidad y al muestreo espacial uniforme del LVM, se detectan en toda la nebulosa numerosas líneas débiles, incluyendo [O III] 4363, [N II] 5755 y He I, lo que permite medir con precisión la morfología de líneas débiles de esta nebulosa. Las tendencias radiales confirman el contenido de polvo notablemente bajo y la homogeneidad global de la temperatura y densidad electrónicas en el anillo principal. La cinemática del gas ionizado trazada por Hα apoya el escenario de una envoltura en lenta expansión realzada en los bordes, en acuerdo con estudios previos. Este trabajo demuestra el poder diagnóstico de la espectroscopía obtenida por el LVM en nebulosas extendidas y su capacidad para recuperar condiciones físicas globales y espacialmente resueltas en estructuras ionizadas complejas.

Corresponding author: Sebastián F. Sánchez *E-mail address:* sfsanchez@astro.unam.mx
Received: January 8, 2026 **Accepted:** February 16, 2026

1. INTRODUCTION

Planetary nebulae (PNe) represent the late evolutionary stages of low- and intermediate-mass stars (1–8 $M_\odot$), tracing the transition from the asymptotic giant branch (AGB) to the white dwarf phase. During this phase, material ejected from the stellar envelope becomes ionized by the increasingly hot central star, giving rise to rich emission-line spectra that provide key diagnostics of physical conditions, ionization structures, and chemical enrichment. Among the nearest and best-studied examples is the Helix Nebula (NGC 7293), whose proximity (~215 pc; Harris et al. 2007) and large angular size (~16′ × 12′) make it an ideal benchmark for

testing spatially resolved photoionization models and plasma diagnostics with high sensitivity.

The Helix has been the subject of extensive spectroscopic investigations over the past five decades, covering the optical, ultraviolet, infrared, and radio regimes. Early studies by Warner & Rubin (1975) and Hawley (1978) established its basic ionization stratification and provided the first integrated measurements of key diagnostic lines such as [O III]5007, [N II]6583, and [S II]6716,6731, relative to Hβ. These efforts revealed a relatively low-ionization nebula with strong [N II] and [O I] emission in the outer zones and a prominent [O III] emission in the central regions, reflecting a significant contribution from partially ionized gas.

Subsequently, Leene & Pottasch (1987) conducted long-slit optical spectroscopy across several positions, demonstrating the strong radial variation of excitation conditions, and elemental abundances. Their results confirmed that helium and oxygen abundances are relatively uniform, while nitrogen and sulfur exhibit gradients consistent with ionization stratification rather than true chemical inhomogeneity[1]. The improved spatial sampling of O'Dell (1998), using narrow-band imaging and region-integrated spectra, revealed substantial structural complexity and confirmed the coexistence of multiple ionization regimes within the nebula, associated with the bright inner ring and fainter outer arcs.

A more quantitative abundance analysis was later provided by Henry et al. (1999), who presented high-quality optical line ratios from three distinct slit positions. Their work remains the reference dataset for chemical abundances in NGC 7293, establishing characteristic values of $12 + \log(O/H) \approx 8.7$ and $He/H \approx 0.11$, comparable to solar abundances but with mild nitrogen enhancement, which is typical of Type II PNe. These studies collectively defined the observational framework against which new, spatially resolved surveys can be compared.

Beyond optical spectroscopy, a wide variety of multi-wavelength observations have further characterized the Helix Nebula. Bublitz et al. (2022) analyzed the molecular and CO chemistry in the outer envelope, tracing the survival of dense knots and their connection to photodissociation regions (PDRs). Etxaluze et al. (2014) presented *Herschel* submillimeter and far-infrared spectra, detecting lines such as OH^+, CO, and [N II]205μm, which probes the transition from ionized to molecular gas. The series of studies by Meaburn et al. (1992, 2005, 2008) and Walsh & Meaburn (1987) focused on kinematics and line profiles (Hα, [N II]), providing detailed insight into the three-dimensional morphology and velocity field of the nebula, albeit without comprehensive line intensity catalogs. More recent works, such as Iskandarli et al. (2024) and Estrada-Dorado et al. (2025), have revisited the properties of the hot central white dwarf and its UV spectrum, while Andriantsaralaza et al. (2020) explored related modeling approaches to planetary nebulae evolution. Together, these studies emphasize that the Helix remains one of the most comprehensively observed planetary nebulae across the electromagnetic spectrum, yet systematic, wide-field optical mapping of its ionization structure is still limited.

Recent wide-field spectroscopic facilities now enable complete, contiguous mapping of extended nebulae with high spatial and spectral fidelity. The Local Volume Mapper (LVM), one of the SDSS-V surveys (Kollmeier et al. 2025; Drory et al. 2024), provides an unprecedented opportunity to revisit nearby planetary nebulae such as the Helix with integral field spectroscopy over degree-scale field. In this work, we present an analysis of the Local Volume Mapper of the Helix Nebula included in the recent SDSS-V 19th Data Release (DR19 SDSS Collaboration et al. 2025), emphasizing the spatially integrated emission-line ratios and their comparison with canonical optical datasets. By benchmarking the LVM measurements against legacy studies from Warner & Rubin (1975) to O'Dell (1998) and Henry et al. (1999), we evaluate both the consistency of derived physical conditions and the extent to which large-scale integral field observations can capture the complex ionization structures of nearby planetary nebulae.

We should highlight the uniqueness of the LVM IFU, which with an angular size of $\sim$0.5′ covers almost the Helix Nebula in a single pointing, sampling it with $\sim$1750 fibers of 35.5″/diameter ($\sim$0.037 pc at the distance of the object). Furthermore, we should note that the analyzed frame is just one of the several exposures that the LVM is taking on this target, which, when combined, will provide much deeper (higher S/N) data that will be delivered to the public in future data releases.

The structure of this article is as follows: in § 2 we describe the LVM observations and data-reduction procedures. § 3 describes the analysis performed, including a brief description of the LVM data analysis pipeline (LVM-DAP), placing an emphasis on the modifications adopted since the previous version (Sánchez et al. 2025). The implemented 2nd order sky correction and the selection of a final sample of high-quality emission lines (golden sample) are described in § 3.1 and § 3.2. The main results of this analysis are presented in § 4, including a description of (i) the distributed dataproducts (§ 4.1), (ii) the integrated and spatially resolved flux intensities of golden sample emission lines (§ 4.2 and § 4.3, respectively), (iii) the radial distribution of the absolute flux intensities (§ 4.4) and their relative values with respect to Hβ(§ 4.4.1), (iv) the ionized gas kinematics (§ 4.5), and (v) the average properties of the stellar population captured within the field-of-view (§ 4.6). The results are discussed in § 5 and the main conclusions of this study are presented in § 6.

2. DATA

The dataset analyzed in this work corresponds to a single pointing of the Helix Nebula (NGC 7293) obtained by the LVM during its commissioning phase at the Las Campanas Observatory in Chile on the night of September 4, 2023. This pointing, identified by the codes MJD = 60191 / Exposure= 4297, was part of the 19th public Data Release (DR19 SDSS Collaboration et al. 2025) of the SDSS-V project (Kollmeier et al. 2025) [2].

The instrumental configuration of the LVM comprises an IFU array fed by four Alt-Az telescopes, one dedicated to science data acquisition (T1, feeds the ultra-wide IFU, 1801 fibers), two monitoring the sky towards East and West (T2 and T3, 59 and 60 fibers, respectively), and one more for observing spectrophotometric calibration stars (T4, 24 fibers). The IFU array consists of DESI-110 like spectrographs covering the 3600 to 9800 Å wavelength range with a spectral resolution of $R \sim 4000$ at Hα. Each spectrograph utilizes a dichroic system to split each fiber beam into three wavelength channels: (b) blue, from 3600 to 5800 Å, (r) red, from 5750 to 7570 Å, and (z) infrared, from 7520 to 9800 Å. The ultra-wide IFU provides detailed spectral and spatial coverage of the survey targets.

The LVM survey Data Reduction Pipeline (DRP; Mejía-Narváez et al., in preparation) follows the procedures described by

[1] It is worth noticing that this may be due to the use of ionization correction factors to account for the unobserved ions, which may depends on the degree of ionization.

[2] https://www.sdss.org/dr19/lvm/

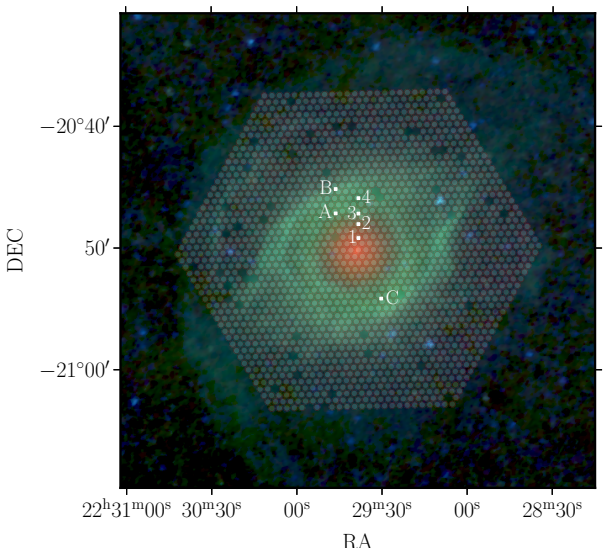

Figure 1. Color image created combining the WISE W4 (22 μm, red), W3 (12 μ, green) and W2 (4.6 μm, blue) band images covering ∼0.65° size centered in Helix Nebula (i.e., a similar FoV of the images explored by O'Dell 1998). The footprint of the LVM science IFU fibers included in the exposure delivered in the SDSS DR19 is represented by a set of semi-transparent white circles. The white points indicate the locations of the regions previously explored in the literature. The regions discussed by O'Dell (1998) are represented by numbers: (1) 'middle', (2) 'transition', (3) 'ring, and (4) 'arc.' Finally, the regions discussed by Henry et al. (1999) are labeled with the same letters adopted in that article.

Sánchez (2006). The pipeline is based on the PY3D reduction package, originally developed for the CALIFA survey (Husemann et al. 2013). Initially implemented in Python 2.7, the code has been upgraded to Python 3.11, and supplemented with dedicated routines specifically designed to address unique characteristics and requirements of the LVM dataset. The current dataset was reduced using DRP version 1.1.1.

Primary processing by the DRP consists of nine stages.

1. preprocessing of raw data frames;
2. identification and tracing of fiber spectra on the CCDs;
3. extraction of spectra;
4. wavelength calibration and linear resampling of spectra;
5. differential correction for fiber-to-fiber transmission variations;
6. flux calibration using data from T4;
7. combination of the three spectral channels into single spectra;
8. night sky background subtraction using data from T2 and T3;
9. computation of astrometric solution using data from guiding cameras.

Throughout the entire reduction process, uncertainties are consistently propagated at every stage.

The final product of this reduction process is a FITS file containing a set of row-stacked spectra corresponding to each LVM pointing, where every row represents an individual science fiber. Separate extensions store the flux intensity, the associated estimated uncertainty, and supplementary information such as the final wavelength solution, the line-of-sight instrumental velocity dispersion (for each fiber and wavelength), masks for bad pixels, flags identifying broken or low-quality fibers and the estimated sky spectrum. An additional extension includes the spatial mapping of each science fiber on the sky (the position table), derived from the astrometric solution, together with further metadata for each fiber (e.g. additional quality masks). This FITS file[3] constitutes the input for the data analysis pipeline, which is described in the following sections.

Figure 1 illustrates the exact location of the pointing in the sky and the field-of-view (FoV) covered by the LVM science Integral Field Unit (IFU). The figure comprises a three-color image covering a ∼0.65° size square area centered on the Helix Nebula, with a similar coverage as the observations discussed by O'Dell (1998). The image was created by combining the W4 (22 μm, red), W3 (12 μm, green) and W2 (4.6 μm, blue) band images obtained by the Wide-field Infrared Survey Explorer (WISE Wright et al. 2010), which were obtained using the Hierarchical progressive surveys tool (HIPS Fernique et al. 2015)[4]. The LVM science fibers included in the exposure analyzed in this study are shown as a set of semi-transparent white circles overlaid on the image. The location of broken/low-quality fibers and the incomplete coverage of the hexagonal IFU FoV is clearly visible in the figure as empty spaces between the fibers. Finally, we highlight the location of regions previously discussed in the literature for future discussion (O'Dell 1998; Henry et al. 1999). Figure 1 clearly shows that most of the extent of the Helix Nebula is covered by the actual pointing, however, the coverage is not 100% complete. There are low intensity regions that are clearly outside the footprint of the explored pointing.

3. ANALYSIS

We apply the LVM Data Analysis Pipeline (LVM-DAP) to the Helix nebula pointing described above. The LVM-DAP was presented and described in detail in Sánchez et al. (2025), and it was distributed publicly [5]. We present here a brief summary, highlighting the modifications introduced since it was first presented. An updated schematic of analysis flow performed by the LVM-DAP is shown in Fig. 2.

The LVM-DAP employs the spectral fitting algorithms implemented in PYFIT3D (Lacerda et al. 2022), a Python 3 package designed to decouple and extract the physical information associated with both the stellar and ionized gas components in integral-field spectroscopic (IFS) data. The LVM-DAP follows the general structure of PYPIPE3D (Sánchez et al. 2016; Lacerda et al. 2022), with specific adaptations to the characteristics of the LVM observations, including the spectral resolution, wavelength coverage, and in particular the nature of the stellar component sampled by each resolution element (fiber). Each individual fiber spectrum is analyzed independently, without spatial binning, ensuring that the spatial information inherent to the LVM's ultra-wide IFU is fully preserved.

The first stage of the analysis focuses on characterizing the stellar continuum. This is achieved by fitting each observed spectrum with a linear combination of templates from a library of RSP (resolved stellar populations). In contrast to the usual analysis performed using other tools such as PYPIPE3D, PPXFS or STARLIGHT (Lacerda et al. 2022; Cappellari & Emsellem 2004; Cid Fernandes et al. 2011), which are based on the stellar synthesis

[3] https://dr19.sdss.org/sas/dr19/spectro/lvm/redux/1.1.1/0011XX/11111/60191/lvmSFrame-00004297.fits
[4] https://aladin.cds.unistra.fr/hips/
[5] https://github.com/sdss/lvmdap

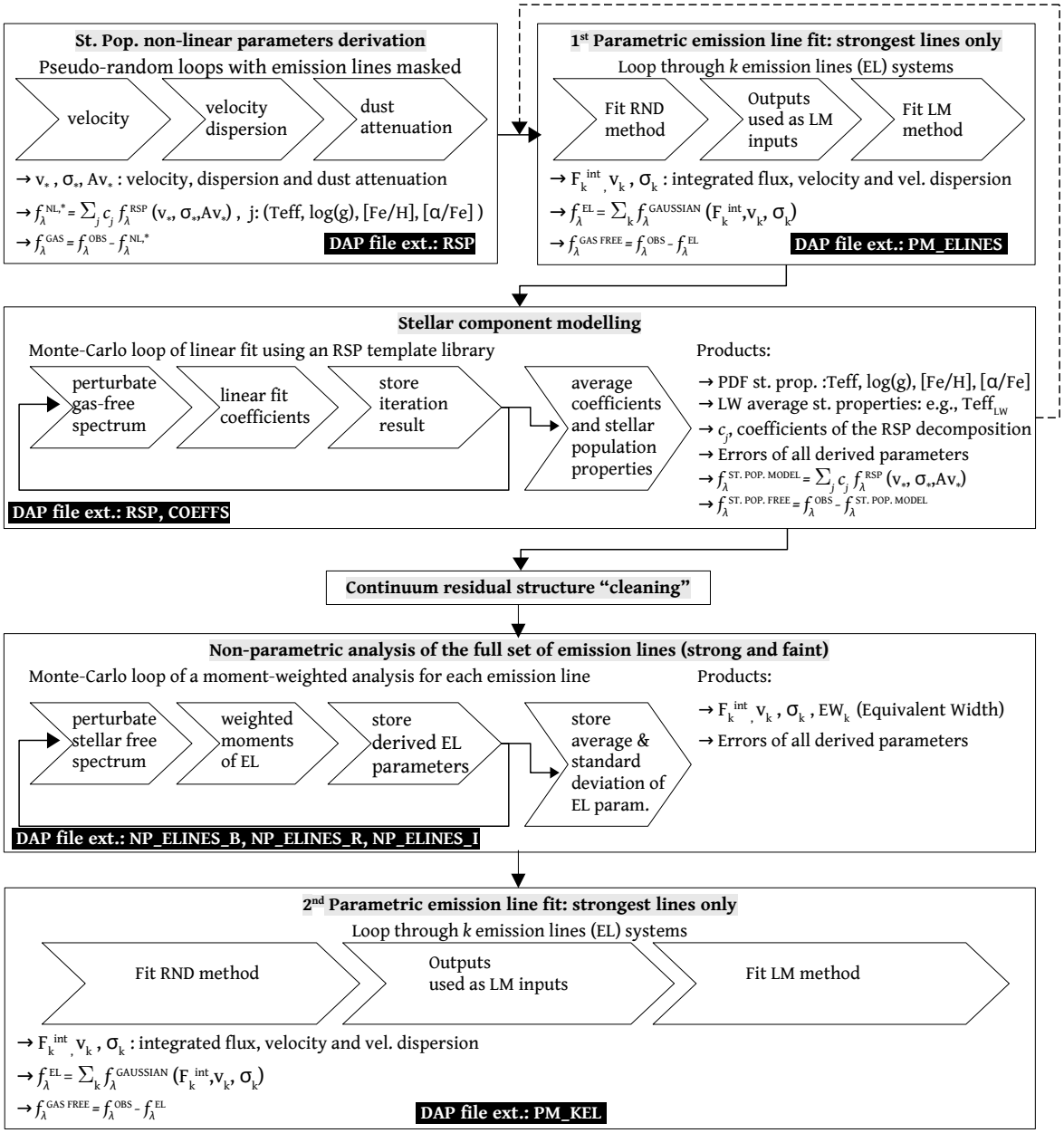

Figure 2. Updated scheme of the LVM-DAP analysis flow for a single fiber spectrum, including the main procedures: (i) derivation of the non-linear parameters of the stellar spectrum ($v_\star$, $\sigma_\star$ and $A_{V,\star}$), (ii) parametric derivation of the properties of the ionized gas emission lines (EL), including the flux intensity (f_{EL}), velocity (v_{EL}) and velocity dispersion (σ_{EL}), (iii) stellar component synthesis, i.e., decomposition into a set of RSP templates, and generating a model of the stellar spectrum, (iv) non-parametric derivation of the properties of the emission lines, including the equivalent width for each emission line (EW_{EL}), and (v) a re-evaluation of the parametric derivation of the emission lines. The last two analyses were performed over a so-called gas-pure spectrum, that is, the residual of subtracting the stellar component model from the original spectrum. RND and LM stand for the two methods included in `pyFIT3D` to fit the parametric models to the EL, as explained in the text. Black boxes indicate in which extension of the DAP data products files the analysis of each module is stored.

method (Bruzual & Charlot 2003; Conroy 2013), each template does not represent the integrated spectrum of a single stellar population (SSP) with a given age, metallicity, and abundance pattern, formed in a single burst of star formation. The varying physical size sampled by the LVM apertures, depending on the distance within the galaxy of the captured targets, and its range of values (from a few to a few hundred of parsecs), does not guarantee a full sampling of the mass function. Thus, the basic hypotheses behind the stellar synthesis method are not guaranteed (e.g. Cerviño et al. 2013). For this reason we introduced the use of RSP, a set of stellar templates, each one representative of a distribution of physical parameters (Teff, log(g), [Fe/H] and [α/Fe]), characterized by a probability distribution function (PDF), minimizing and controlling the degeneracies in the space of observed parameters (i.e., the spectra). The details of how the RSP templates are defined and created are also explained in Sánchez et al. (2025). For the current analysis we adopted a set of RSP templates created based on the MaStar stellar library (Yan et al. 2019), classified using the CoSha code (Mejia-Narvaez et al. 2021), which are distributed in the LVM github repository.

Two distinct RSP template libraries are employed in the LVM-DAP. The first one, optimized for efficiency, is used to derive the non-linear parameters that characterize the stellar kinematics and dust attenuation (v_*, σ_*, and $A_{V,*}$). This first library is deliberately small to minimize computational cost and degeneracies, comprising 12 RSP templates in the current analysis. During this analysis, which performs a pseudo-random brute-force exploration of the space of the non-linear parameters within a pre-defined range of values, the strongest emission lines were masked.

This procedure provides a first/preliminary model of the stellar spectrum. This stellar model is used to create a continuum-subtracted, gas-pure spectrum, which is used to create a first model of the emission lines (following the procedure described below). This emission line model is then subtracted from the original spectrum to create a gas-free spectrum. This spectrum is then fitted using a second, more extensive RSP library, covering a finer grid of stellar properties and adopting the nonlinear parameters derived in the first step (comprising 108 templates in the current analysis). In this way, the best stellar model, the coefficients of the decomposition, and the light-weighted average of the stellar properties were derived (see Fig. 2).

The DAP characterizes the emission lines using two complementary procedures: (i) a *parametric* Gaussian fitting of the strongest emission lines, providing integrated flux ($F_{\rm int}$), velocity ($v_{\rm gas}$), and velocity dispersion ($\sigma_{\rm gas}$) for each line system; and (ii) a *non-parametric* moment-weighted analysis applied to the large set of emission lines, delivering fluxes, velocities, dispersions, and equivalent widths (EW). The parametric analysis comprises 15 emission lines, while the non-parametric analysis currently including 215 emission lines. In the current version of the LVM-DAP (v1.1.0), the parametric analysis is performed twice (contrary to the previously published version Sánchez et al. 2025): the first time after the derivation of the non-linear parameters of the stellar population, and the second time after the derivation of the best stellar model using the full RSP library. The results of both analyses are stored and delivered separately in the final dataproducts. On the contrary, the non-parametric analysis is performed only once, using the best stellar model to create the gas-pure spectrum and adopting as initial guess values the results of the 1st parametric analysis (see Fig. 2).

In addition to the double evaluation of the properties of the emission lines based on the parametric analysis, the current version of the LVM-DAP has introduced an estimation, for each explored emission line, of (i) the velocity dispersion in units of km s^{-1}, corrected by the instrumental LSVD provided by the DRP for each fiber and wavelength, and (ii) the corresponding reduced χ^2. These two values are derived for both parametric (2nd evaluation) and non-parametric analyses. For the former, the χ^2 is derived by just evaluating the final model using the derived parameters. For the non-parametric method we assume that the line profile follows a Gaussian function using the values derived by this procedure. The results are stored in a new table included in the LVM-DAP dataproducts, together with the adopted instrumental LSVD for each emission line.

Prior to running the full fiber-by-fiber analysis, the DAP analyzes an integrated spectrum obtained by coadding all science-fiber spectra of the pointing, weighted by their inverse variance. First, the average redshift/velocity within the considered frame is derived by performing a cross-matching of the observed wavelength of Hα and [N II] doublet with their rest-frame counterparts. This derivation of the velocity is used to readjust the range of explored the parameters in any subsequent analysis. Then, the full analysis described above, following the scheme outlined in Fig. 2 was applied to the integrated spectrum. The results of this analysis are used to define reliable initial guesses and parameter ranges for both the stellar and ionized gas components for the full analyzed dataset, improving the accuracy and the stability of the individual fits.

The results of this analysis are presented in Fig. 3. The integrated spectrum is shown together with the best fit model for the underlying stellar population and the model for the emission lines analyzed using the second iteration of parametric procedures. The spectrum has been divided into the three wavelength ranges covered by the three arms of the spectrograph, with a set of insets highlighting (i) the strongest emission lines within the considered wavelength range, (ii) three particularly relevant wavelength ranges for the stellar population analysis (centered on the K+H Ca doublet, Hβ and the CaT), and (iii) the wavelength ranges centered on the three most relevant auroral lines ([O III]4363, [N II]5755 and [S III]6312). A visual inspection of this figure clearly highlights the existing problems with the sky subtraction in the currently released dataset, reduced using DRP version 1.1.1. The multiple apparent absorptions (and emissions) at any wavelength, but in particular in the regime corresponding to the infrared arm, are a clear consequence of this problem. This is significantly improved in the newer versions of the DRP (above version 1.2.0), currently under development, particularly after introducing a correction for telluric absorption. This issue is primarily affecting the stellar continuum, which is very weak and not very suitable for a proper stellar decomposition. This will be discussed in the following sections. However, despite these problems the nebular emission lines analyzed using the parametric procedure presents a very good S/N and accurate modeling. Furthermore, even some weak features, such as the auroral lines shown in the maps, have sufficient signal-to-noise levels to allow the determination of the physical parameters of the ionized nebulae (e.g., electron temperature). We should note here that this distributed dataset corresponds to a frame taken during the science commissioning of the instrument, when the full observing procedure (including the sky estimation) adopted along the formal survey period was still not in place and it was reduced with an under-development version of the DRP. A spectrum more representative of the current quality of the LVM data was presented in Sánchez et al. (2025), Sattler et al. (2025), González-Torà et al. (2025), Villa-Durango et al. (2025) and Hilder et al. (2025).

Throughout all steps of the analysis, uncertainties are propagated via Monte Carlo simulations that perturb the input fluxes according to the errors provided by the DRP. Thus, for each of the physical parameters delivered by our analysis, there is an associated error. How these errors are representative of real uncertainties is discussed in Sánchez et al. (2025).

3.1. Night Sky 2nd Order Correction

As indicated before, the analyzed dataframe presents some defects due to imperfect sky subtraction (e.g. Fig. 3). Our current understanding of this problem is that it arises from a combination of a problem in the estimation of the night-sky spectrum itself and an imperfect estimation of the fiber-to-fiber transmission correction (Mejía-Narváez et al., in preparation). We acknowledge this problem in the data reduction applied to the publicly accessible frame which is indeed properly addressed in under-development versions of the DRP. For the current dataset

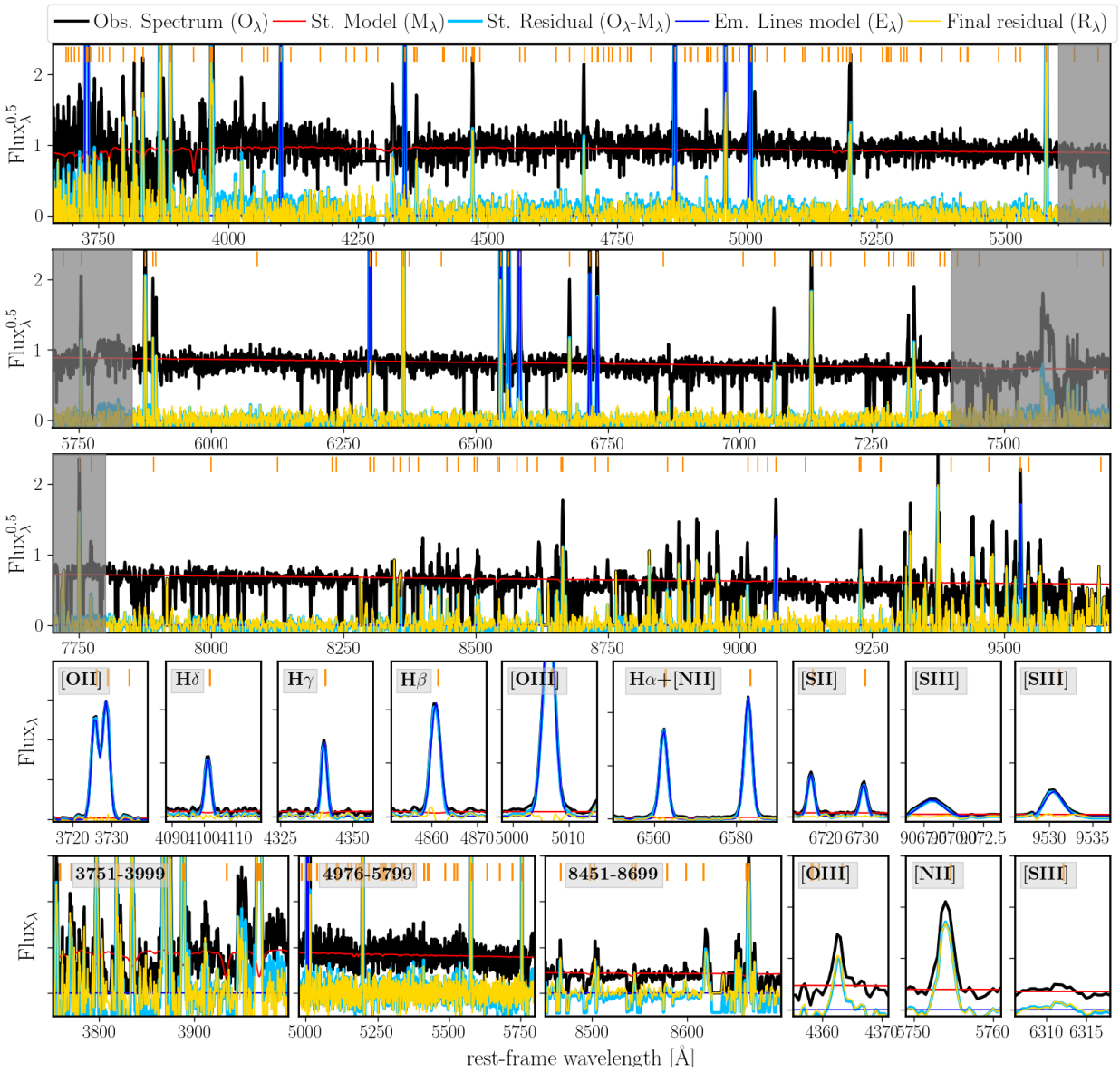

Figure 3. Integrated spectrum of the Helix Nebula across the entire field-of-view of the analyzed LVM pointing (black solid line), together with the results from the LVM-DAP analysis, i.e., the best-fitting stellar model (red solid line), the model of the strongest emission lines fitted with Gaussian functions (blue solid line), the residual after subtraction of the stellar model (cyan solid line), and the combination of both models, including a final correction to the residual shape (yellow solid line). The first three panels, from top to bottom, display the wavelength ranges covered by the blue (1st row), green (2nd row), and infrared (3rd row) arms of the LVM spectrograph. The shaded areas indicate the overlapping regions between the arms. The insets in the two bottom rows show zoom-ins for the selected wavelength intervals. The panels in the 4th row illustrate the quality of the modeling for the strongest emission lines based on the parametric analysis described in the text. Finally, the bottom row of panels presents three wavelength ranges (3751–3999 Å, 4976–4799 Å, and 8451–8699 Å) that highlight the specific spectral features discussed in the text. Three additional insets display close-ups around the auroral lines most commonly used to determine the electron temperature in ionized nebulae: [O III] λ4363, [N II] λ5755, and [S III] λ6312. The flux scales in these three insets are identical to facilitate a comparison among the lines. In all panels, orange vertical lines indicate the emission lines analyzed using the non-parametric procedure described in the text.

we present an *a posteriori* correction for those emission lines that are clearly affected by this issue, which we present here.

First, we select two regions within the FoV of the IFU (Dec>-20.57° or Dec<-21.0°), corresponding either to areas of low-intensity (for the strong emission lines) or those that should corresponds directly to the night sky emission. For each emission line we determined the median flux intensity (med_{f-back}) within these two regions along with the corresponding standard deviation (σ_{f-back}). For those emission lines in which (i) the median flux is above a certain threshold in units of the standard deviation (n_σ; this means there is a non-negligible signal) and (ii) the standard deviation is below an additional threshold, lim_σ (to avoid structure in the detected signal, separating it from a homogeneous background contribution), we subtract med_{f-back} from the flux intensity of the considered emission line for all fibers. The n_σ and lim_σ values (1.5 and 10^{-13} erg s^{-1} cm^{-2}) were the same for

[5]We note that different approches, including the an average and a set of weighted-average was explored before deciding to adopt this final approach.

Table 1. Description of the DAP file containing the dataproducts of the analysis.

HDU	EXTENSION	# Rows	# Columns
0	PRIMARY		
1	PT	#spec	6
2	RSP	#spec	1 + #RSP
3	COEFFS	#spec × #RSP	13
4	PM_ELINES	#spec × #PM_EL	10
5	NP_ELINES_B	#spec	1+#NP_EL_B ×8
6	NP_ELINES_R	#spec	1+#NP_EL_R ×8
7	NP_ELINES_I	#spec	1+#NP_EL_I ×8
8	PM_KEL	#spec × #PM_EL	10
9	ELINES_SIGMA_CHI	#spec	2(2#PM_EL+#NP_EL)
10	ELINES_CHI2_AVG	2#PM_EL+#NP_EL	4
11	INFO	#param	2

Structure of extensions included in the delivered DAP file, where: (i) #spec is the number of science spectra (or fibers) included in the analyzed `Tile` or RSS (row-stacked spectra) frame; (ii) #RSP is the number of templates/spectra included in the stellar library; (iii) #PM_EL is the number of individual models (emission lines) included in the parametric analysis of the ionized gas emission lines, and (iv) #NP_EL_BAND is the number of emission lines included in the non-parametric analysis for each BAND (B, R and I) corresponding to each arm of the spectrograph, and (v) #NP_EL is the total number of emission lines analyzed using the non-parametric procedure.

all emission lines, being selected in an iterative process in which med_{f-back} of the corrected lines are minimized.

The described correction was derived for all the emission lines. However, for only four of the 215 analyzed lines does it produce a non-negligible effect (i.e., a modification above the noise level): [N II]5755, [O I]6300, [O I]6364, and HI8665. These lines are among the most relevant (and well explored in previous literature) to explore the ionization structure and the physical properties of the nebula and its physical properties, what justifies the described correction. Furthermore, it is worth noticing that in the case of N II5755, the background bias is not homogeneous across the FoV, showing a pattern clearly associated to the six fiber-bundles that configure the LVM science IFU (Herbst et al. 2024). For this particular case the med_{f-back} is subtracted only in those regions in which, a clear background excess intensity is evident.

In Appendix A.1 we show an example of the effect of the described the correction for a particular emission line.

3.2. Emission lines Golden Sample

Once this correction is performed we explore which lines among the 215 analyzed were detected above the background noise. For doing so we select two circular apertures of 3′ located at (i) the central region of the nebula (-20.775° , 337.450°), and (ii) a region corresponding to the brightest area of the nebular ring (-20.850° , 337.400°). These two areas are selected acknowledging the different spatial distribution expected for different emission lines arising from different ionizing regions within the nebula. We then obtain the median flux intensity in both apertures (med_{f-neb}), together with the integrated flux intensity and its corresponding error across the entire FoV. We mark as good detections those emission lines in which (i) $med_{f-neb} > 1.5\sigma_{f-back}$ for any of the considered regions, and (ii) the integrated flux intensity is at least three times its error (≈3σ detection). These dual criteria are selected to guarantee not only a sufficient S/N in the integrated quantities, but that the detected flux corresponds to areas actually covered by the nebula. A total of 54 emission lines fulfill both criteria (i.e., ∼26% of the original analyzed set of emission lines). We define this sub-set as our emission line golden sample.

4. RESULTS

4.1. DAP dataproducts

The main result of this exploration is the set of dataproducts derived by LVM-DAP for the analyzed exposures. These dataproducts are delivered as a multi-extension FITS-file (the DAP file[6]), comprising a set of FITS-tables in which there are stored the different parameters (and errors) for each science fiber, and some additional extensions comprising relevant information about the analyzed the pointing and parameters adopted during the analysis.

The format has already been described by Sánchez et al. (2025). For the currently delivered data product, each extension comprises (i) the header of the original dataframe for traceability (`PRIMARY`), and a set of FITS tables including (ii) the mapping or position table of each science fiber on the sky (`PT`), (iii) the luminosity weighted average values of the physical properties of the stellar component derived by the stellar decomposition process (`RSP`), (iv) the actual weights obtained in this decomposition required to reconstruct the stellar spectral model and generate the PDF of the stellar properties (`COEFFS`, and the properties of the emission lines derived by (v) the 1st analysis using the parametric fitting process (`PM_ELINES`), (vi) the non-parametric procedure, separated in each spectrograph arm (`NP_ELINES_B`, `NP_ELINES_R` and `NP_ELINES_I`, (vii) the 2nd analysis using the parametric procedure (`PM_KEL`), (viii) the velocity dispersion corrected by instrumental resolution in km s^{-1} and the reduced χ^2 of the fitting to each emission line (`ELINES_SIGMA_CHI`), (ix) the actual instrumental resolution correction applied and the average reduced χ^2 for each analyzed emission line (`ELINES_CHI2_AVG`), and finally (x) a table including all the configuration parameters adopted to run the LVM-DAP in the current analysis (`INFO`).

Table 1 summarizes the format of the delivered DAP file, describing the size of each extension. It is important to note that all tables included in each extension containing dataproducts (all but `PRIMARY` and `INFO`) contain a column with a unique key (`id`) built using the exposure number of the observed frame (`EXPNUM`, 4297 in this particular case), and the identification number of the analyzed fiber in the original `SLITMAP` extension provided by the DRP (`FIBERID`). This way, id = EXPNUM.FIBERID, is

[6] https://ifs.astroscu.unam.mx/LVM_DR19_Helix/Helix_DR19_new.dap.fits.gz

Table 2. Integrated flux intensities of the Helix Nebula emission line golden sample.

Name	λ^1	flux^2	name	λ^1	flux^2	name	λ^1	flux^2
[OII]	3726.03	4693.4 ± 4.7	[FeII]	4474.91	99.1 ± 18.3	HeI	6678.15	128.4 ± 3.4
[OII]	3728.82	6142.6 ± 4.4	HeII	4685.68	248.1 ± 3.5	[SII]	6716.44	403.2 ± 4.2
HI^3	3797.90	228.2 ± 7.7	[ArIV]	4711.33	27.9 ± 2.6	[SII]	6730.82	290.0 ± 1.8
HeI^3	3819.61	154.7 ± 29.2	HeI	4713.14	18.8 ± 2.8	HeI	7065.19	85.3 ± 2.0
HI^3	3835.38	249.7 ± 19.9	Hβ	4861.36	2382.1 ± 7.8	[ArIII]	7135.80	560.9 ± 1.5
[NeIII]	3868.75	2100.8 ± 6.0	[OIII]	4958.91	3690.3 ± 83.9	[OII]	7318.92	131.6 ± 3.4
HeI^3	3888.65	637.4 ± 3.4	[OIII]	5006.84	11820.9 ± 25.5	[CaII]	7323.88	75.0 ± 2.9
HI^3	3889.05	613.4 ± 3.4	[NI]	5197.90	126.6 ± 2.0	[OII]	7329.66	116.0 ± 2.4
HeI^3	3964.73	72.1 ± 3.5	[NI]	5200.26	146.7 ± 2.0	[ArIII]	7751.06	163.7 ± 4.7
[NeIII]^3	3967.46	752.4 ± 2.9	HeII	5411.52	15.9 ± 4.6	HeII	8236.77	11.3 ± 1.6
CaII^3	3968.47	633.9 ± 3.1	[FeII]	5412.64	14.8 ± 4.6	HI	8239.24	6.9 ± 1.7
Hϵ^3	3970.07	463.4 ± 3.0	[NII]	5754.59	120.2 ± 3.2	HI	8598.39	14.0 ± 2.0
HeI	4026.19	78.0 ± 10.2	HeI	5876.00	460.2 ± 2.6	[CI]	8727.13	37.1 ± 4.7
Hδ	4101.77	642.9 ± 4.6	[OI]	6300.30	854.6 ± 7.0	HI	8750.47	59.0 ± 2.0
Hγ	4340.49	1067.1 ± 5.4	[OI]	6363.78	283.2 ± 15.5	HI	8862.78	59.8 ± 4.1
[OIII]	4363.21	51.9 ± 7.4	[NII]	6548.05	3717.6 ± 68.8	[SIII]	9069.00	169.1 ± 3.2
HeI	4471.48	144.9 ± 7.6	[NII]	6583.45	11206.8 ± 22.8	HI	9229.02	62.9 ± 0.7

(1) Wavelength is expressed in Å; (2) flux intensity is expressed in 10^{-13} erg s^{-1} cm^{-2}. All fluxes are based on the LVM-DAP non-parametric analysis; (3) Emission-lines which a χ^2 three times larger than the average, which flux derived using the non-parametric procedure has to be taken with care, as it could be blended with other nearby emission lines or night-sky residuals.

a unique identification key for a particular fiber corresponding to a particular location in the sky observed in a particular LVM exposure. Using this `id` it is very easy to either combine the content of the different tables, using it as a key parameter to join columns, and/or combine the dataproducts derived from different exposures. For instance, to create mosaics, as those shown in Figures 8 to 11 of Drory et al. (2024), or to combine dithered observations.

In addition to the standard DAP file, we deliver the result of the background correction described in § 3.1[7]. Contrary to the previous file this comprises a single FITs table in which the unique `id` described before is included, along with the `RA` and `Dec` describing the position of the fiber in the sky, and the corrected flux intensities of the considered emission lines. We should stress that this is not a standard LVM-DAP product as the implemented *a posteriori* correction would not be required when the updated version of the DRP is implemented.

4.2. Integrated emission line fluxes

As indicated in § 3 the analysis that comprises the LVM-DAP is first applied to an inverse-variance weighted integrated spectrum (see Fig. 3). This procedure provides same set of parameters included in the DAP-file described in § 4.1 for this integrated spectrum. However, due to the weighting procedure those values may not be directly adopted as a good representation of the real integrated properties of the considered exposure, in this particular case of the Helix Nebula. A better set of values is obtained by coadding the flux intensities included in the different emission line extensions included in the DAP file (see Table 1).

Table 2 lists the integrated flux intensities derived from this analysis. There are few studies that report the absolute integrated fluxes for this nebula, and certainly none that provides measurements for the complete list included here. Early observations using narrow-band imaging reported an integrated flux for [O III] and Hβ of $F([\mathrm{O\,III}]\,\lambda5007) = 19.4 \times 10^{-10}$ and $F(\mathrm{H}\beta) = 3.37 \times 10^{-10}$ erg cm^{-2} s^{-1} (O'Dell 1998), superseding an earlier measurement of $F(\mathrm{H}\beta) = 4.5 \times 10^{-10}$ erg cm^{-2} s^{-1} by O'Dell (1962). For these two emission lines, our LVM integrated spectrum yields $F([\mathrm{O\,III}]\,\lambda5007) = 11.82 \times 10^{-10}$ erg cm^{-2} s^{-1} and $F(\mathrm{H}\beta) = 2.38 \times 10^{-10}$ erg cm^{-2} s^{-1}, respectively. Thus, the LVM absolute fluxes are lower than the historical full-nebula values by $\sim$ 39% for [O III] 5007 and $\sim 29 - 47\%$ for Hβ. On the other hand, the line ratio derived using the LVM values, $F([\mathrm{O\,III}]\,\lambda5007)/F(\mathrm{H}\beta) = 4.96$ is within the two historical values, 4.3 and 5.8, differing by only $\sim$ 15%. The LVM-IFU FoV, with a hexagonal area of $\sim$0.45°^{2}, covers most of the optical extent of the nebula, and certainly the brightest regions. However, it is still smaller than the area covered by the discussed narrow-band images: a rectangular FoV of $\sim$0.65° size (O'Dell 1998), covering an area of $\sim$1.17°^{2} (i.e., $\sim$2.6 times larger). Besides that, the filling factor of the LVM-IFU, considering fibers of 35.3″, is $\sim$83%. The combined effect of a smaller FoV and the non-complete filling factor may well explain this discrepancy.

A rough estimation of the flux lost due to these effects could be obtained by comparing the integrated flux of the WISE W3-band image included in Fig. 1 with the one observed through the LVM science fibers. The emission at $\sim12\mu$m traces the Hα luminosity, following a correlation that it is frequently used to explore the integrated SFR in galaxies (e.g. Leroy et al. 2021; Colombo et al. 2025). This correlation holds irrespective of the photoionizing source, as the physical nature of the connection between both emissions is the same: the ultraviolet emission that produces the ionization is the one that it is reprocessed and emitted at FIR because of dust. Based on this analysis we estimate $\sim$31% of lost flux, which is reasonably in agreement with the reported discrepancy.

The values reported in Table 2 correspond to the non-parametric analysis, a procedure that it is not optimized to handle the possible contamination by nearby blended emission lines or night-sky residuals. We have labeled all those lines that could be affected by this effect in Table 2, based on the χ^2 of the comparison of the gas-pure spectra with a Gaussian model created using parameters derived from the non-parametric procedure. This effect may be

[7] https://ifs.astroscu.unam.mx/LVM_DR19_Helix/Helix_DR19_cor.fits.gz

more pronounced for weak emission lines located near much stronger ones (e.g. CaII3968 instead of Hε). The reported fluxes for these lines should be considered carefully.

4.3. Spatial distribution of the ionized gas

Figure 4 shows the flux intensity maps of the 20 brightest emission lines included in the *golden sample* defined in § 4.2 and listed in Table 2 (for the remaining lines, the maps are included in Appendix A.2). The observed spatial distributions reveal the complex ionization structure of the Helix Nebula, highlighting the characteristic morphology produced by the interaction between the ionizing radiation from the central star and expanding nebular gas. The overall appearance of the nebula is dominated by a bright annular structure encircling a lower-surface-brightness core, which is surrounded by fainter, more diffuse emission that extends into the outer halo. The different emission lines display distinct spatial morphologies, reflecting the stratification of ionization states within the nebula.

Maps of different Balmer lines (for example, Hα Hβ, Hγ and Hε), which trace the distribution of the ionized hydrogen, effectively delineate the full extent of the ionized gas. Their relatively smooth brightness across the main ring indicates that the Balmer emission primarily arises in regions of moderate ionization, where hydrogen is almost fully ionized; however, helium is only singly ionized. The strong contrast between the bright inner ring and the fainter outer halo suggests that the density of the ionized gas peaks within this structure, which likely represents the intersection of a moderately inclined ionization front with the plane of sky.

The [O III]5007 emission, the brightest emission line among those observed in the LVM dataset, displays a slightly concentrated distribution toward the inner portions of the main ring. This behavior reflects the dependence of the O^{++} ion on the availability of photons with energies above 35 eV (Osterbrock & Ferland 2006), which are abundant near the central star (Osterbrock & Ferland 2006; O'Dell 1998; Meaburn et al. 2005; O'Dell et al. 2007). The resulting [O III] morphology thus traces zones of high excitation, corresponding to gas fully ionized in hydrogen and helium but not yet depleted of O^{++} through further ionization. The enhanced [O III] emission observed in the inner parts of the ring likely marks the transition between the He^{++} and He^{+} regions, where the local electron temperature reaches its maximum as a result of efficient photoelectric heating, and reduced cooling efficiency. Similar distributions are observed in other high excitation emission lines, like [Ar III]7136, [S III]9069, or [S III]9531.

In contrast, emission lines like [N II]6583, [O II]3727, and [S II]6717,31, highlight the low-ionization structures that lie at and beyond the main ring (e.g. Meaburn et al. 2005). For these emission lines the brightest regions are found along the outer boundary of the [O III] bright ring, where the ionization front is tangential to the line of sight. Nitrogen, oxygen and sulfur are singly ionized in these regions (e.g. N^{+}), coexisting, most probably, with neutral He and partially ionized H. The enhancement of [N II] emission along filamentary features and knot-like structures, described by O'Dell (1998), suggests the presence of dense condensations that are externally photoionized and shielded from the most energetic photons, leading to the observed sharp transition between the high- and low-ionization zones.

The HeII4686 line outlines a compact, centrally concentrated region surrounding a hot central star. Similar patterns are found for the other He II lines included in the golden sample (HeII5411 and HeII8237), despite being considerably weaker. This morphology indicates that the emission originates within the He^{++} zone, where helium is fully ionized by photons with energies exceeding 54.4 eV (e.g. Osterbrock & Ferland 2006). The circular symmetry of the HeII distribution, and its confinement well inside the [O III] ring, support the scenario in which the ionizing continuum is dominated by a very hot central star whose hard radiation field maintains a small but bright He^{++} volume in the inner nebula (O'Dell 1998; O'Dell et al. 2007; Henry et al. 1999). The relative faintness of this feature compared to other emission lines, like [O III], Hα or Hβ is consistent with the limited solid angle subtended by this high-excitation core (Gruenwald & Viegas 1992; Tylenda et al. 2003).

Finally, the HeI6678 emission line delineates the region of intermediate ionization between the compact He^{++} core and the low-ionization peripheries. This line arises from the recombination of singly ionized helium and trace zones where hydrogen was fully ionized. However, helium remains only partially ionized (e.g. Osterbrock & Ferland 2006). Its morphology closely follows that of Balmer lines, but it peaks slightly inward, indicating the spatial extent of the He^{+} zone produced by photons with energies between 24.6 and 54.4 eV (e.g. Peimbert & Torres-Peimbert 1983; Benjamin et al. 1999). The smooth distribution of HeI emission across the main ring suggests that most of the nebular volume is maintained in this intermediate ionization state, consistent with a central star that provides a hard, yet not extreme, ultraviolet radiation field. The relative strength of HeI6678 further supports a He^{+}/H^{+} abundance ratio of about 0.1, typical of a nebula where helium is nearly fully ionized throughout the main body (Benjamin et al. 1999; Peimbert et al. 2017). Indeed, this was the helium abundance reported for the Helix Nebula in previous studies (Kingsburgh & Barlow 1994).

In addition to the dominant bright annular structure discussed above, the emission line maps in Fig. 4 reveals two secondary morphological components. First, a fainter but clearly defined inner ring-like feature is visible in some of the strongest emission lines, including Hα, Hβ, and [O III]5007. This structure delineates the boundary of the central cavity surrounding the hot central star and is interpreted as the inner edge of the ionized shell, where the line of sight becomes tangential to the cavity wall. The second distinct feature is the low-ionization "arm" located in the north-western quadrant of the nebula, which stands out prominently in the [N II]6583, [O II]3729, and [S II]6716,6731 doublet. This structure traces material at larger radii than the main [O III] ring and is consistent with externally illuminated, lower-excitation gas associated with the outer ejected layers of the nebula. Its enhanced low-ionization emission suggests higher local densities and partial shielding from the hardest ionizing photons, conditions that favor the survival of N^{+}, O^{+}, and S^{+} ions. Both structures have been reported and discussed in earlier studies of the Helix (e.g. O'Dell 1998; Henry et al. 1999; Meaburn et al. 2005).

In summary, the observed distribution of the discussed emission lines demonstrates that the spatial morphology of the Helix Nebula arises naturally from its three-dimensional ionization structure (O'Dell 2005). The emission-line stratification reflects both the spectral hardness of the central star and the projection of the ionization front through a geometrically thick inclined disk-like shell. These features are consistent with a photoionization-dominated nebula where variations in local density and geometry modulate the observed brightness distribution across different ionic species, as already discussed in

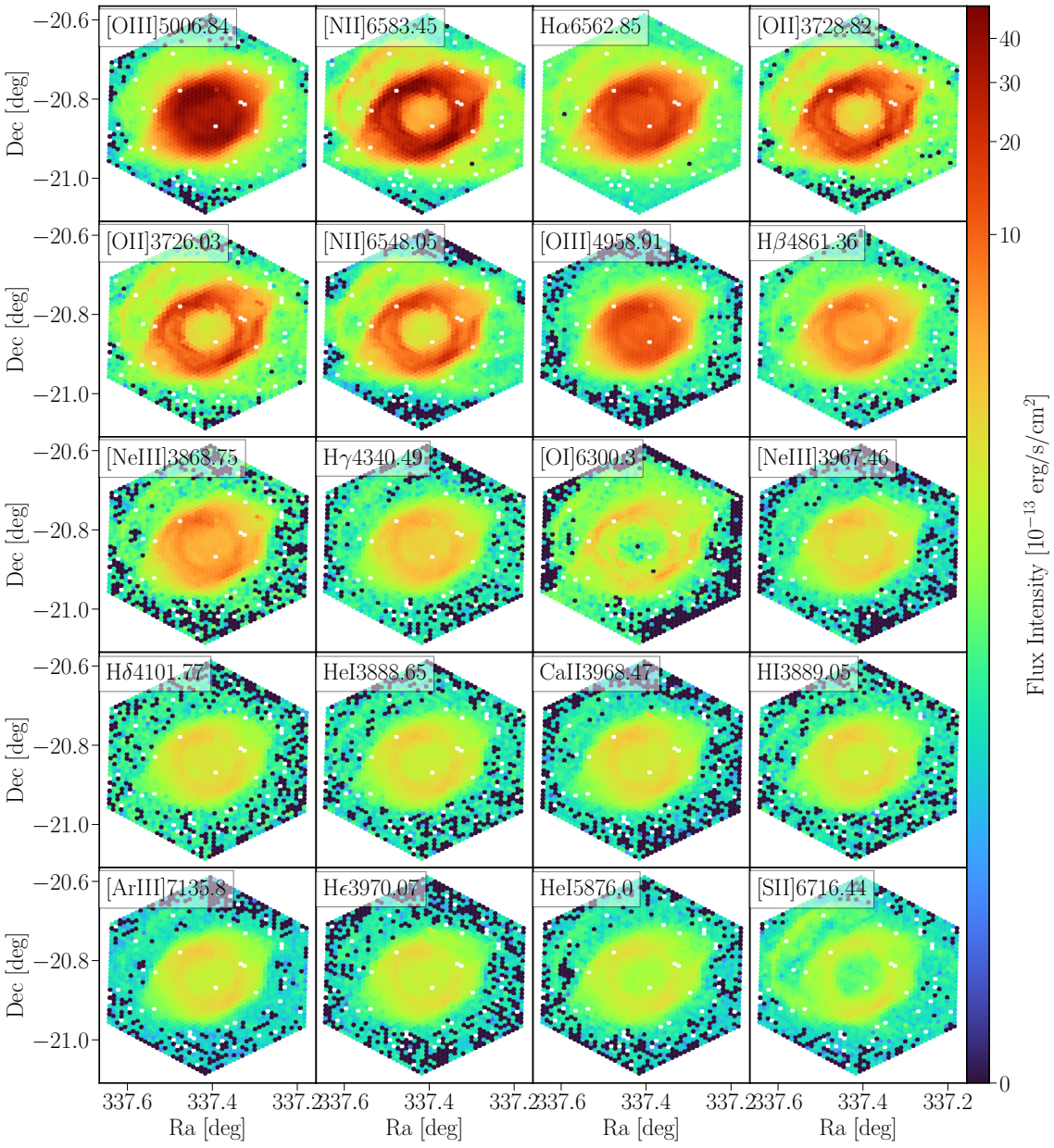

Figure 4. Example of the analysis performed by LVM-DAP to recover the properties of the ionized gas emission lines. Each panel shows the distribution across the FoV of the LVM IFU of the flux intensity estimated by the weighted-moment procedure for the 20 brightest emission lines shown in the integrated spectrum of the Helix Nebula(Fig. 3). The emission lines are ordered from the brightest (top left) to the faintest (bottom right). The legends in each panel indicate the emission lines. The remaining detected emission lines are shown in Appendix A.2

previous studies (e.g. O'Dell 1998; Henry et al. 1999; O'Dell et al. 2007).

4.4. Radial distribution of emission line fluxes

In previous sections we have determined that the nebula presents, to first order, a spherical ionization structure, with a central ionizing source (a PN hot star). Therefore, it should be well characterized by the radial distribution of the observed emission lines. Figure 5 (left panel) shows the azimuthally averaged radial profiles of the flux intensities for a representative subset of the emission lines. These profiles were obtained by deriving the mean and standard deviation of the fluxes within a set of circular annuli of 0.5′ width centered at the location of the central white dwarf that ionizes the nebula. For all lines (and line ratios), there is a very small dispersion around the mean value at any radial distance. This feature, per se, strengthens the proposed scenario in which the ionization structure is well represented by a spherical, highly symmetrical distribution.

The radial behavior of the Balmer lines (Hα, Hβ, and Hγ) closely follows the overall surface brightness of the nebula, with a broad maximum corresponding to the main ring and a smooth decline toward the inner cavity and outer halo. This morphology confirms that the hydrogen recombination emission traces the full extent of the ionized gas, as discussed in § 4.3. The gradual variation of their intensities with radius indicates that the ionized hydrogen remains nearly homogeneous within the main ring,

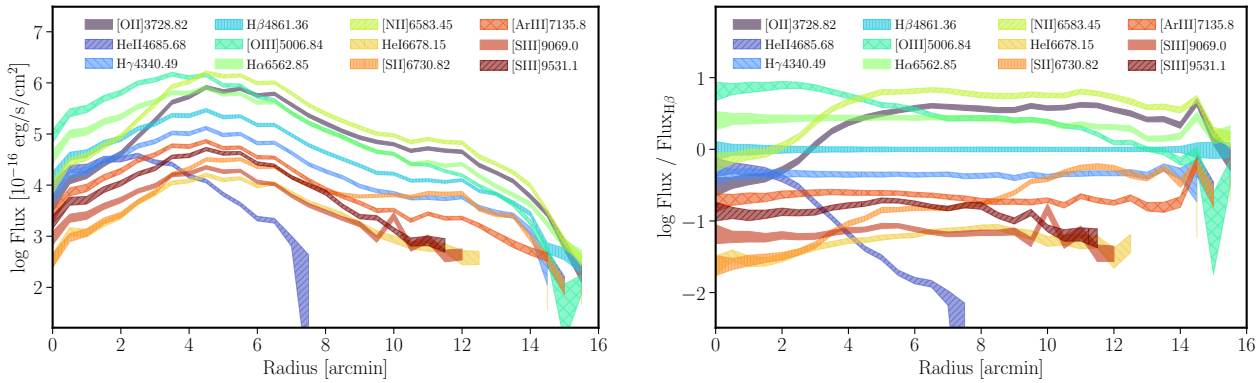

Figure 5. Radial profiles of the azimuthally averaged flux intensities in each fiber in absolute values (left-panel), and relative to Hβ (right-panel), for a sub-set of the emission lines analyzed along this study. The filled region in each profile corresponds to the standard deviation across the radial bin of 0.5′. Each emission line is represented by a different color and hash style. The sub-set comprises both prominent hydrogen recombination lines (Hα, Hβ, Hγ), and key collisional excited transitions ([O II]3737, [O III]5007, [N II]6584, [S II]6731, [Ar III] and [S III]9069,9531) that trace the ionization structure of the nebula. The profiles reveal the characteristic bright main ring around ∼5′–7′ and the decline toward the outer halo, highlighting the differences in excitation between high- and low-ionization species. Similar structure is seen in Fig. 4.

consistent with a photoionization-dominated structure in which density variations dominate over temperature gradients (e.g. O'Dell 1998; Henry et al. 1999; Meaburn et al. 2005; O'Dell et al. 2007).

High-ionization species such as [O III]5007 or [S III]9069,9531 exhibit more peaked profiles toward the inner portions of the nebula (with [O III]5007 being the most centrally peaked emission). Their maxima occur at smaller radii than those of the Balmer lines, confirming the strong excitation gradient inferred from two-dimensional maps. This concentration reflects the dependence of the O^{++} and S^{++} ions on photons with energies above ∼35 eV (assuming a constant gas density), which are abundant only close to the central star (Osterbrock & Ferland 2006; O'Dell 1998). The smooth decline of these lines outward suggests a gradual softening of the radiation field with increasing distance, as the high-energy photons are absorbed by the inner gas layers (e.g. Mellema 1995; Schönberner et al. 2005).

In contrast, low-ionization lines such as [N II]6583, [O II]3729, and [S II]6731 peak at larger radii, delineating the ionization front at the outer boundary of the main ring (consistent with the distribution shown by the Balmer lines). Their enhanced emission coincides with the regions where the ionization front becomes tangential to the line of sight (e.g. O'Dell 1998), as seen in spatial maps (Fig. 4). These lines trace ionized zones with a low degree of ionization, where N, O, and S are singly ionized and coexist to a large extent with neutral helium, as described in the imaging analyses of O'Dell (1998) and the spectroscopic studies of Meaburn et al. (2005); O'Dell et al. (2007). The contrast between the inner [O III] maximum and the outer [N II]/[S II] enhancement reflects the classical ionization stratification expected in a photoionized shell illuminated by a hot central star (e.g. O'Dell et al. 2007).

The HeII4686 line shows a compact distribution with a sharp central maximum, confirming its origin within the innermost He^{++} zone (O'Dell 1998; Henry et al. 1999; O'Dell et al. 2007). On the other hand, intermediate-ionization species such as HeI6678 display radial profiles that peak well beyond those of the HeII4686 and the Balmer lines, consistent with emission from the He^{+} zone that fills most of the nebular volume (e.g. Peimbert & Torres-Peimbert 1983; Benjamin et al. 1999; Peimbert et al. 2017). The agreement between these radial trends and the morphological patterns described in the previous section demonstrates the consistency between the integrated and spatially resolved analyses, reinforcing the hypothesis of a nearly spherically symmetric ionization structure.

4.4.1. *Emission line fluxes relative to Hβ*

The right panel of Fig. 5 displays the corresponding line ratios, normalized to Hβ, as a function of radius for the same emission lines shown in the left panel. As in the case of the fluxes themselves, the line ratios present a very small azimuthal dispersion around the mean value at each radial distance. This supports the scenario in which the ionization presents a spherical structure.

The Balmer ratios (Hα/Hβ, Hγ/Hβ, and Hδ/Hβ) remain remarkably constant as a function of the radius across the entire nebula. The absence of significant radial variations indicates that internal dust extinction within the ionized shell is either extremely low or uniformly distributed. This behavior is consistent with earlier optical analyses of the Helix Nebula, which also found negligible or spatially uniform reddening (e.g. O'Dell 1998; Henry et al. 1999; Meaburn et al. 2005).

Because the intrinsic Case B Balmer ratios are only mildly sensitive to density and temperature in the typical nebular regime, the observed flatness of the radial profiles suggests that the physical conditions throughout the ionized gas do not exhibit extreme variations—of at least one order of magnitude—on the spatial scales probed by the LVM ultra-wide IFU. A detailed determination of the temperature and density structures is beyond the scope of this study. We will address this in future studies using additional pointings obtained by the LVM survey of the Helix Nebula (Orozco-Duarte et al., in preparation).

Beyond the Balmer emission lines, the remaining line ratios displayed in the right-hand panel of Fig. 5 reveal systematic radial trends that mirror the ionization stratification already identified in the two-dimensional maps (§ 4.3) and in the flux profiles of the left panel. High ionization ratios, such as [O III]5007/Hβ, exhibit a pronounced peak toward the inner regions, reflecting the concentration of O^{++} in zones exposed to the hardest radiation field near the central star. This behavior is fully consistent with the compact morphology of He II λ4686 and with the enhanced [O III] emission inside the main ring. The gradual decline of these

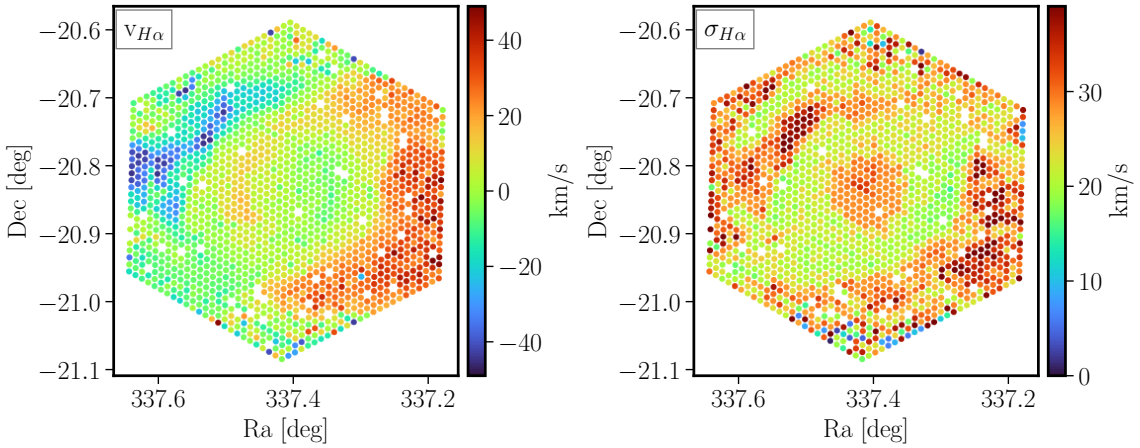

Figure 6. Spatial distribution of the Hα velocity (left-panel) and velocity dispersion (right-panel) derived using the 2nd parametric analysis of the emission lines by the LVM-DAP for the analyzed Helix Nebula dataset. The velocity map shows a blue-/red-shift pattern with a maximum absolute velocity coincident with the highest velocity dispersions, in agreement with an spherically expanding shell.

ratios with increasing radius, sharper for the He line, indicates a softening of the ionizing continuum as high-energy photons are progressively absorbed in the inner nebular layers, as described above.

Intermediate-excitation ratios, such as He I λ6678/Hβ or [Ar III]7136/Hβ, show a broader plateau across the main ring, reaching their maximum, where the He^+ zone is most extended. Their slow radial variation reflects the fact that these ions dominate over a large volume of the nebula, consistent with the relatively smooth morphology observed in their two-dimensional maps. On the contrary, low-ionization ratios, such as [N II]6583/Hβ, [O II]3727/Hβ, and [S II]6717,6731/Hβ, rise steeply toward outer nebula, peaking just beyond the [O III] bright ring. This behavior echoes the enhancements seen in their spatial maps, where these lines trace the edge of the ionization front and the clump-dominated low-ionization structures. The outward increase in these ratios reflects the transition from hydrogen-ionized gas to partially ionized or neutral material and confirms the classical ionization stratification of Helix Nebula. The coincidence of their maxima with the projected location of the ionization front agrees with earlier studies that associate these low-ionization lines with dense knots and filamentary structures in the outer ring, as discussed previously (e.g. O'Dell 1998; Meaburn et al. 1992).

4.5. Ionized gas kinematics

Figure 6 shows the observed velocity[8] ($v_{H\alpha}$) and velocity-dispersion ($\sigma_{H\alpha}$) maps derived for the Hα emission line, extracted from the 2nd parametric analysis of the emission lines described in § 3, which traces the bulk kinematics of the ionized gas throughout the inner 40′ of the Helix Nebula. The line-of-sight velocity map reveals a smooth, large-scale gradient with a clear redshifted–blueshifted symmetry along a preferential axis. This structure is consistent with the projection of a slowly expanding, moderately inclined shell, as previously inferred from long-slit spectroscopy and Fabry–Perot interferometry (Meaburn et al. 1992; Walsh & Meaburn 1987; O'Dell 1998). The approaching (blueshifted) region lies to the northwest, whereas the receding (redshifted) region extends to the southeast, consistent with earlier determinations of the nebula's orientation and dynamical axis (e.g. O'Dell 1998; Meaburn et al. 2005). The measured velocity amplitudes, ∼33 km s^{-1}, align with previous estimates for the global expansion of the ionized shell (Henry et al. 1999; O'Dell et al. 2004), confirming that the Helix remains a relatively low-velocity, evolved planetary nebula.

The Hα velocity-dispersion map, once corrected by the intrinsic velocity dispersion as described in § 3, shows enhanced values toward the inner cavity and along the brightest sections of the main rings. Lower dispersions were observed in the outer regions. These narrow line widths (typically $\sigma_{H\alpha}$ ∼10-15 km s^{-1}) are consistent with thermal broadening at electron temperatures of T_e ∼10^4 K plus a modest contribution from unresolved turbulent motions, matching previous detailed studies (Henry et al. 1999; O'Dell et al. 2007). Slightly broader profiles in the inner regions coincide with the line-of-sight integration of the front and back sides of the expanding shell, an effect commonly observed in planetary nebulae with hollow or cavity-type geometries (e.g. Gruenwald & Viegas 1992; Tylenda et al. 2003).

The combined velocity and dispersion maps support the interpretation that the Helix Nebula traces the limb-brightened edges of a thick, slowly expanding, quasi-spherical bubble(e.g. O'Dell et al. 2007). This dynamical structure is a natural outcome of the canonical interacting stellar wind model for planetary nebulae, in which fast winds from the hot central star sweep up the previously ejected AGB envelope into an expanding ionized shell (e.g. Osterbrock & Ferland 2006). The velocity field extracted from Hα mirrors the signatures expected from such a geometry: redshift–blueshift symmetry, enhanced line splitting toward the nebular center, and moderately increasing dispersions where the shell is intersected along longer sight-lines. These properties are in strong agreement with classic kinematic analyses of the Helix and other evolved nebulae (e.g. O'Dell 1998; Meaburn et al. 2005; O'Dell et al. 2007).

The kinematical patterns recovered from the LVM data closely resemble those reported in earlier high-resolution optical studies, including the global expansion velocity of ∼20-30 km s^{-1}, the inclination of the ring-like structure, and the mild internal turbulence inferred from linewidth (Walsh & Meaburn 1987; Meaburn et al. 1992, 2005). The excellent agreement demonstrates

[8] not corrected by Heliocentric velocity

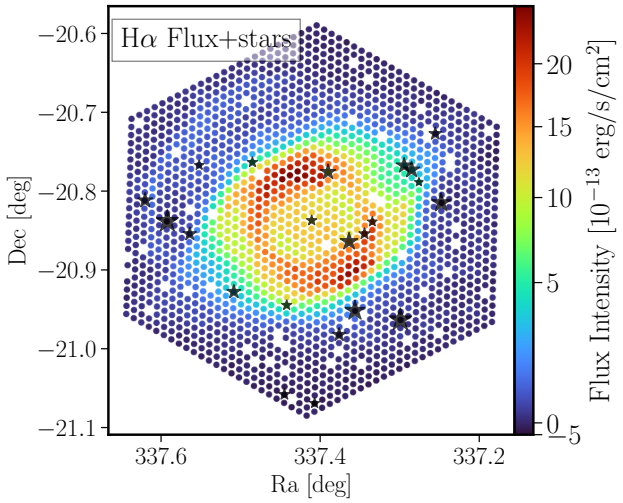

Figure 7. Distribution across the FoV of the fibers in which the stellar spectra have a S/N>5 at ∼5500 (solid stars) together with the Hα intensity map (already shown in Fig. 4) in arbitrary units, which was used as spatial references. The size of the stars corresponds to the S/N, ranging from ∼5 for the faintest ones to ∼30 for the brightest. The central star of the Helix Nebula has a S/N just above 5.

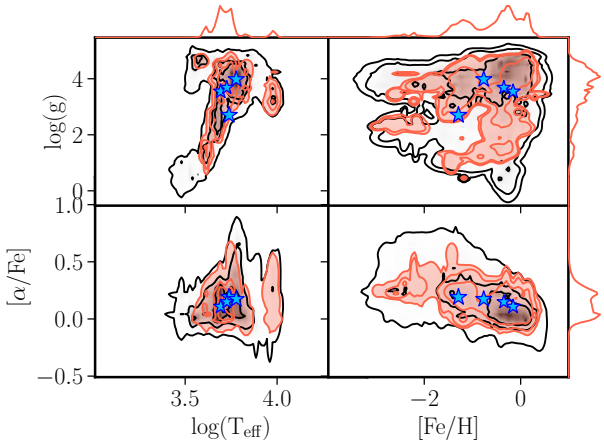

Figure 8. Probability distribution function of the physical properties of stars (T_{eff}, log(g), [Fe/H] and [α/Fe]) for the full RSP template comprising 108 RSPs (black contours), together with the same distribution for the four stars in the FoV with a S/N>25 (see Fig. 7 based on the DAP analysis. Each panel shows the PDFs for a pair of physical properties: T_{eff}-log(g) (top-left); [Fe/H]-log(g) (top-right); T_{eff}-[α/Fe] (bottom-left) and [α/Fe]-[Fe/H] (bottom-right). In each panel, each successive contour corresponds approximately to 1, 2, and 3σ. The histograms in the top and right panels show the projected PDFs for each parameter. The luminosity-weighted values for each of the four stars are represented by blue stars.

that the wide-field LVM observations reliably capture the large-scale dynamical structure of this prototypical planetary nebula.

4.6. Stellar population content

As summarized in § 3, and described in detail in Sánchez et al. (2025), the LVM-DAP models the stellar spectra by decomposing them into a set of RSP templates, stellar spectra characteristic of a particular distribution of physical properties that minimize the degeneracies among them. This type of analysis provides reliable results when the signal-to-noise ratio reaches a certain threshold that depends strongly on the number of templates considered in the decomposition. For the currently assumed RSP library, which comprises 108 templates, this minimum S/N is ∼40-50, based on simulations (Sánchez et al. 2025). Below this threshold, the procedure provides a model for the underlying stellar component; however, the estimated physical parameters are not completely reliable. Nevertheless, the configuration adopted for the current analysis performs this decomposition when S/N>20. Below this limit, if S/N>1, the procedure only looks for the single RSP that best fits the underlying continuum. In other cases, the underlying continuum is ignored in the analysis.

The LVM exposure analyzed along this study, centered on the Helix Nebula, was acquired during the science commissioning explorations with the main aim of exploring the ionized ISM, and it was never intended to obtain high-quality S/N spectra of the stellar content in the (projected) vicinity of the nebula. Thus, neither the central ionizing star nor the field stars present a particularly high S/N. Figure 7 shows the distribution within the FoV of the 22 fibers in which the stellar spectra have S/N >5 at 5000Å for the analyzed dataset. Only four of them present a S/N >25, and none are sufficiently bright to provide reliable decomposition of the stellar content. In particular, the fiber covering the central star presents a low S/N, ∼6.

Nevertheless, as the main purpose of the current exploration is to provide a showcase of the analysis provided by the LVM-DAP, describing the content of the dataproducts presented in § 4.1, we present here the results of the stellar decomposition for the four fibers with higher S/N. Figure 8 shows the PDF of the stellar properties derived combining the results of the DAP decomposition for these spectra, projected in the log(g)-Teff, log(g)-[Fe/H], [α/Fe]-Teff, and [α/Fe]-[Fe/H] planes, are compared with the distribution for the full MaStar stellar library (as described in Sánchez et al. 2025). The luminosity-weighted average values for the four fibers are included for comparison. We should stress that this stellar component corresponds to field stars that we cannot confirm to be related in any way with the studied nebula, and that the results, due to limited S/N values are not reliable. Therefore, we refrain from making any discussion or extracting any conclusion on the results presented. For an example of a direct connection between the stellar component and the ISM observed by LVM, we refer the reader to Villa-Durango et al. (2025). In this recent study, the authors illustrate the power of these data, unveiling the spatially resolved interplay between ionized gas, molecular material, dust, and stellar content in the Rosette Nebula across large angular scales.

5. DISCUSSION

The single exposure taken by the LVM of the Helix Nebula distributed in the SDSS DR19 provides one of the deepest and most spatially complete optical spectroscopic data sets ever obtained for this object. A particularly compelling demonstration of the capabilities of the survey is the detection of faint auroral and high-excitation diagnostic lines across a very large field of view. Figure 9 illustrates this clearly, showing a direct comparison between the spatial distribution of bright nebular lines such as [O III]5007, Hα, [N II]6583, and the much weaker counterparts [N II]5755, Hϵ and [O III]4363. These lines typically reach intensities of ∼0.5-2% of Hβ in classical long-slit observations, and in some cases even lower, making them notoriously difficult to measure reliably over extended regions. Nevertheless, both bright and weak lines trace a similar distribution within the nebula.

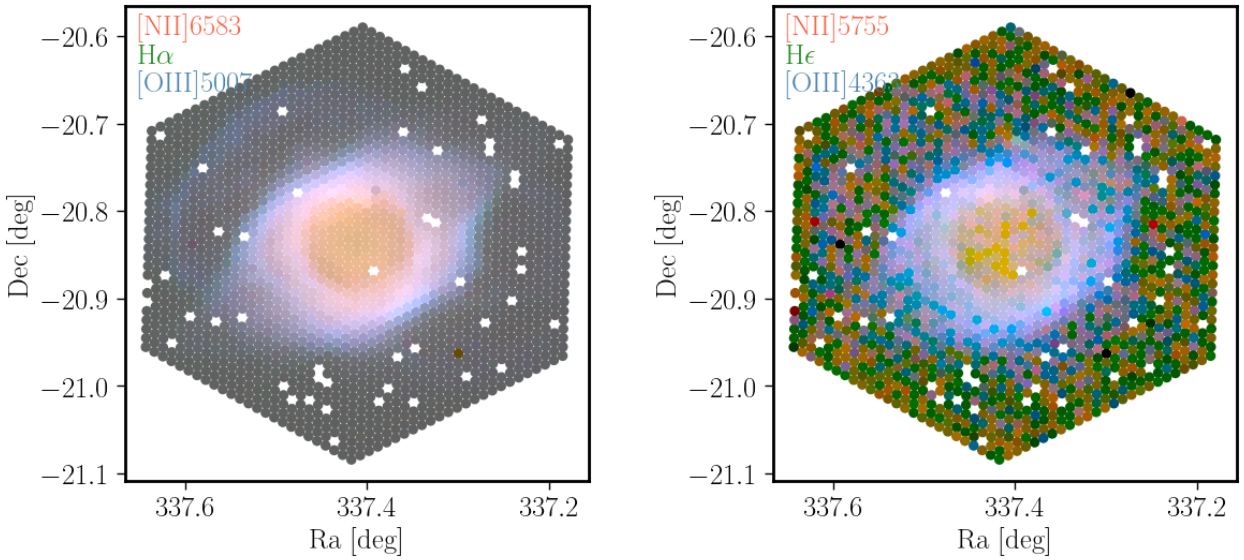

Figure 9. *Left-panel:* Distribution of the fluxes recovered by the DAP for the [O III] λ5007 (blue), Hα (green), and [N II] λ6583 (red) strong emission lines using the non-parametric analysis for the analyzed pointing on the Helix Nebula. *Right panel:* Similar distribution as the one shown in the left panel for the [O III] λ4363 (blue), Hϵ (green), and [N II] λ5755 (red) weak emission lines. The fluxes are displayed using arbitrary intensity scale chosen to enhance contrast, using the same scaling for the three emission lines considered in each figure.

Table 3. Emission line fluxes across the Helix Nebulae: comparison with the literature.

Emission Line (λ)		O'Dell (1998)			Henry et al. (1999)			LVM pointing
(Å)	(1)	(2)	(3)	(4)	(A)	(B)	(C)	(Integrated)
[O II] 3727	103	143	328	674	188	518	718	454.8
He II 4686	61.2	45.6	20.3	4.6	8.9	3.3	0.46	10.4
[O III] 4959	259	293	284	190	209	167	81	155.0
[O III] 5007	754	841	818	551	714	507	309	496.2
[N II] 6548	40.4	33.1	77.1	186	81	150	280	156.1
Hα 6563	270	281	278	288	272	286	284	277.1
[N II] 6583	74.1	100	243	575	250	465	842	470.4
[S II] 6717	3.1	4.0	4.9	12.6	3.6	9.2	22	16.9
[S II] 6731	2.1	2.7	3.4	8.9	2.6	6.6	16	12.2
[O I] 6300	2.6	6.3	9.1	22.5				35.9[1]
[O I] 6363	0.8	2.8	3.3	7.9				11.9[1]
He I 5876	10.0	12.5	14.7	18.2	15	17	17	19.3

Fluxes are normalized to Hβ=100 10^{-13} erg s^{-1} cm^{-2}. (1) Emission lines possible affected by imperfections in the sky subtraction, as discussed in the text.

Figure 9 shows that both [O III]4363 and [N II]5755 are coherently detected even in regions where the surface brightness drops by several orders of magnitude relative to the bright central ring for the strongest lines (e.g. [O III]5007). This spatial robustness, not achievable with earlier slit- or aperture-based studies, is essential for constraining temperature variations and potential small-scale thermal inhomogeneities throughout the nebula (e.g. Kreckel et al. 2024; Sattler et al. 2025; Sarbadhicary et al. 2025, Méndez-Delgado et al., in preparation; Egorov et al., in preparation; Singh et al., in preparation). The recovery of such weak features across more than thousands of independent fibers results from the combination of wide-field IFU coverage (~0.45°[2]), the size of the fibers projected in the sky (~35.3″), stable spectrophotometric calibration, accurate sky subtraction intrinsic to the LVM instrument and survey design, and the capabilities of DRP. This is achieved despite the remaining imperfections of the sky subtraction, as discussed in § 3. The ongoing improvements in the development of the DRP suggests not only the resolution of this issue but also a clear improvement in the final depth achieved by the same observations (Mejía-Narváez et al. in preparation).

As indicated in the manuscript, several previous observations have explored the Helix Nebula, using narrow-band imaging and focused slit-spectroscopy. Table 3 provides a quantitative comparison between the LVM line ratios and a subset of those published in classical studies (e.g. O'Dell 1998; Henry et al. 1999). We should recall that the exact location from which those values

were extracted was already shown in Fig. 1. Overall, the LVM values fall within the range spanned by previous measurements, despite the large diversity of apertures, slit widths, and extraction geometries employed in the historical literature, particularly when the spatial (radial) variations of the different line fluxes (and ratios) are considered (e.g. Fig. 4 and 5). For example, the LVM [O III]5007/Hβ ratio lies between the inner and outer apertures reported by O'Dell (1998), consistent with the fact that the LVM footprint covers both high- and intermediate-ionization zones, projected on the sky. Similarly, the intensities measured for [O III]4363 and [N II]5755 agree with earlier determinations by Leene & Pottasch (1987) and Henry et al. (1999), validating the accuracy of the LVM flux calibration even at levels 100-1000 times fainter than the Hβ level.

Where differences appear, they are clearly attributable to spatial variations within the nebula and to differences in the apertures and their locations in classical studies. Earlier spectroscopic measurements were obtained through narrow slits or small circular apertures, sampling either the inner cavity or the bright ring, whereas the LVM ratios represent area-averaged values over a large, contiguous hexagonal footprint. Because the Helix nebula exhibits strong ionization stratification, the integrated values naturally differ from those derived from discrete, spatially limited regions. The systematic behavior observed in Fig. 5 and the comparisons included in Fig. 9 and Table 3 reinforce this interpretation: lines arising from high-excitation species (e.g. He,II,4686, [O III],4363) present lower integrated/average values across the nebula body (i.e., LVM values) than in the inner-aperture measurements of O'Dell (1998), whereas low ionization features (e.g. [N II],5755, and [O I],6300) are enhanced compared to the values obtained from apertures centered on the cavity. This trend is precisely what is expected for a geometrically thick, nearly face-on planetary nebula dominated by an ionization-bounded main ring, which is the general scenario described in this study.

The combined results therefore demonstrate two fundamental outcomes of the LVM observations: (i) the data reach a depth and spatial uniformity that allow weak diagnostic lines to be mapped across the full nebular extent with high fidelity, which is unattainable in previous optical spectroscopic studies of NGC 7293; and (ii) the consistency of the LVM line ratios with historical measurements, once aperture effects are accounted for, validates the accuracy of the LVM-DRP and confirms that the Helix Nebula's canonical ionization structure, as inferred from decades of long-slit and narrow-band work, is fully reproduced by the new dataset. These results highlight the unique capability of the LVM to combine spectroscopic depth with true wide-field coverage, enabling a comprehensive spatial characterization of nebular excitation, temperature, and density conditions in a manner that was not previously possible.

A further strength of this analysis lies in the performance of the LVM Data Analysis Pipeline (LVM-DAP), which is specifically optimized to recover both strong and extremely weak emission features across tens of thousands of independent spectra. The combination of robust stellar-continuum subtraction, iterative Monte Carlo error propagation, and dual parametric and non-parametric emission-line measurements ensures that faint diagnostic lines, such as [O III] 4363, [N II] 5755, and high-order Balmer lines, are extracted with statistically meaningful uncertainties, even at very low equivalent widths, as predicted by Sánchez et al. (2025).These capabilities, combined with the excellent homogeneity of the spectrophotometric calibration provided by the LVM instrument, demonstrate that the DAP can reproduce the classical nebular diagnostics and significantly improves the spatial completeness and sensitivity compared to previous studies.

6. CONCLUSIONS

In this work, we present a detailed spectroscopic analysis of a single SDSS-V Local Volume Mapper (LVM) pointing of the Helix Nebula (NGC 7293) obtained during science commissioning. Despite being acquired in an early phase of operations, and reduced with a pipeline still under development (Mejía-Narváez et al., in preparation), the data demonstrate the remarkable sensitivity, spatial completeness, and spectrophotometric stability of the LVM system, enabling a comprehensive view of the ionized-gas structure across the bright ring, central cavity, and inner halo of one of the nearest planetary nebulae.

The spatial distributions of the main nebular emission lines reveal the expected ionization stratification of a photoionized, moderately inclined shell: high-excitation species such as [O III]5007 peak in the inner portions of the main ring, intermediate-ionization tracers such as He,I,6678 follow closely the morphology of the Balmer emission, and low-ionization lines such as [N II]6583, [S II]6717,6731, and [O II]3727 delineate the outer ionization front, associated knots, and filaments. These results are fully consistent with classical narrow-band imaging (e.g. O'Dell 1998; Meaburn et al. 2005; O'Dell et al. 2007) and provide the first fiber-by-fiber spectroscopic mapping across the entire nebula.

The radial analysis reinforced the results derived from the 2D maps, with azimuthally averaged flux profiles showing that each ionic species peaked at the radius expected from its ionization potential. Balmer lines remain remarkably constant in their ratios relative to Hβ, indicating that dust extinction is extremely low and spatially uniform, and that the nebular electron temperature and density vary only modestly across the observed field. These results echo previous slit-based determinations of the homogeneous physical conditions in the Helix (e.g. Henry et al. 1999), while offering a panoramic view that is not accessible to earlier observations.

One of the major capabilities highlighted in this study is the ability of the LVM to detect very faint auroral lines across the entire field. The detection of temperature-sensitive auroral lines on a fiber-by-fiber basis is unprecedented for a Galactic planetary nebula at this angular scale. The excellent agreement between our integrated line ratios and those from earlier long-slit studies (O'Dell 1998; Henry et al. 1999) validates both the data quality and the performance of the LVM-DAP.

The ionized gas kinematics further support the classical interpretation of the Helix as a slowly expanding, quasi-spherical shell whose limb-brightened geometry reproduces both the velocity pattern and line width distribution observed across the field. The global kinematic signature agrees with previous Fabry-Perot and high-resolution spectroscopic studies (e.g. Meaburn et al. 2005), demonstrating that even in its commissioning stage, the LVM delivers reliable velocity information at native spatial sampling.

Taken together, these results establish the LVM as a transformative instrument for spectroscopic studies of nearby extended nebulae. The combination of large areal coverage, uniform spectrophotometry, and sensitive DAP extraction enables simultaneous access to bright diagnostics, faint auroral lines, and spatially resolved kinematics across tens of thousands sightlines. The present analysis of the Helix Nebula serves as a proof of concept for the scientific return expected from the full LVM survey, which will provide an unprecedented census of ionized gas structures throughout the Milky Way and Local Volume.

SFS acknowledges the support by CBF-2025-I-236 project granted by the Secretaría de Ciencia, Humanidades, Tecnología e Innovación (SECIHTI) of the Mexican Federal Government, and the PID2022-136598NB-C31 (ESTALLIDOS) Grant from the Spanish Ministry of Science and Innovation (MCINN). JEMD, CM, SFS, ROD, LS, JT and CRZ thank the support by SECIHTI CBF-2025-I-2048 project "Resolviendo la Física Interna de las Galaxias: De las Escalas Locales a la Estructura Global con el SDSS-V Local Volume Mapper" (PI: Méndez Delgado). G.A.B. acknowledges support from the ANID Basal Project FB210003. J.G.F-T gratefully acknowledges the grant support provided by ANID Fondecyt Postdoc No. 3230001 (Sponsoring researcher), the Joint Committee ESO-Government of Chile under agreement 2023 ORP 062/2023, and the support of the Doctoral Program in Artificial Intelligence, DISC-UCN. KK gratefully acknowledges funding from the Deutsche Forschungsgemeinschaft (DFG, German Research Foundation) in the form of an Emmy Noether Research Group (Grant number KR4598/2-1, PI Kreckel) and the European Research Council's starting grant ERC StG-101077573 ("ISM-METALS"). OE acknowledges funding from the Deutsche Forschungsgemeinschaft (DFG, German Research Foundation), project ID 541068876.

Funding for the Sloan Digital Sky Survey V has been provided by the Alfred P. Sloan Foundation, the Heising-Simons Foundation, the National Science Foundation, and the Participating Institutions. The SDSS acknowledges the support and resources provided by the Center for High-Performance Computing at the University of Utah. The SDSS telescopes are located at the Apache Point Observatory, funded by the Astrophysical Research Consortium and operated by the New Mexico State University, and at the Las Campanas Observatory, operated by the Carnegie Institution for Science. The SDSS web site is www.sdss.org.

SDSS is managed by the Astrophysical Research Consortium for the Participating Institutions of the SDSS Collaboration, including the Carnegie Institution for Science, Chilean National Time Allocation Committee (CNTAC) ratified researchers, Caltech, the Gotham Participation Group, Harvard University, Heidelberg University, The Flatiron Institute, The Johns Hopkins University, L'Ecole polytechnique fédérale de Lausanne (EPFL), Leibniz-Institut für Astrophysik Potsdam (AIP), Max-Planck-Institut für Astronomie (MPIA Heidelberg), Max-Planck-Institut für Extraterrestrische Physik (MPE), Nanjing University, National Astronomical Observatories of China (NAOC), New Mexico State University, The Ohio State University, Pennsylvania State University, Smithsonian Astrophysical Observatory, Space Telescope Science Institute (STScI), the Stellar Astrophysics Participation Group, Universidad Nacional Autónoma de México, University of Arizona, University of Colorado Boulder, University of Illinois at Urbana-Champaign, University of Toronto, University of Utah, University of Virginia, Yale University, and Yunnan University.

APPENDICES

A.

A.1. Effects of the 2nd order sky correction

As described in § 3.1 the imperfect sky-subtraction performed by version 1.1.1 of the DRP produces an overestimation of the flux intensities for a handful of emission lines for which we are required to perform an *ad hoc* 2nd order sky correction. Figure 10 illustrates this effect on the spatial distribution of the flux intensities for two different emission lines: [N II]6548, which is barely or not affected, and [O I]6300, which is clearly affected. The maps on the top panels are extracted from the original DAP file [9], while those in the bottom panels are extracted from the file storing the corrected flux intensities [10]. Like the rest of the figures included in this manuscript, this figure was created using the notebooks included in the GITHUB repository[11].

The imperfect sky subtraction in the upper-left panel produces a high background intensity that creates an apparently uniform plateau in the outer FoV regions. Visual inspection of the uncorrected spatial distributions for the [N II]6548 and [O I]6300 flux intensities suggests a background excess in the 2nd emission line. This is confirmed by the exploration of the relative line ratios with respect to Hβ, which provide non-physical values for [O I]6300, much larger than the values previously reported in the literature (e.g. Table 3). In contrast, the distribution of the corrected flux intensities followed the expected pattern, with values of the same order as those reported in the literature. We should stress that (i) this contamination by a non-perfect sky subtraction affects a very limited number of emission lines that lie very nearby (or exactly at the same wavelength) of well-known strong sky emission lines and (ii) the source of this problem has been identified and corrected in the currently developing version 1.2.0 of the DRP. Thus, we do not expect this effect to be present in the future data released by the LVM survey.

A.2. Emission line intensity maps

As already indicated in § 4.3, the flux intensities for the 20 brightest emission lines included in the *golden sample* are shown in Fig. 4. Figures 11 and 12 show the spatial distribution of the flux intensities for the remaining 36 emission lines in descending order of integrated flux intensity. As discussed along the text, the observed spatial distributions reveal the ionization stratification of the Helix Nebula: (i) Strong-ionization lines trace mostly the annular ring, being more peaked at the inner regions, (ii) Low-ionization lines are distributed along larger radial distances, following a shallower gradient, and (iii) Emission lines that require higher excitation energies (e.g. HeII or [Fe II]) are confined within the nebular ring, with a sharp intensity drop.

B. SOFTWARE DISTRIBUTION

In order to facilitate the use the dataproducts delivered by the DAP, and in particular those delivered in the current exploration, we deliver the python notebooks used to create all the figures shown along this manuscript [12]. Details on how to read the entire DAP file

[9] https://ifs.astroscu.unam.mx/LVM_DR19_Helix/Helix_DR19_new.dap.fits.gz
[10] https://ifs.astroscu.unam.mx/LVM_DR19_Helix/Helix_DR19_cor.fits.gz
[11] https://github.com/sfsanchez72/Helix_DR19
[12] https://github.com/sfsanchez72/Helix_DR19

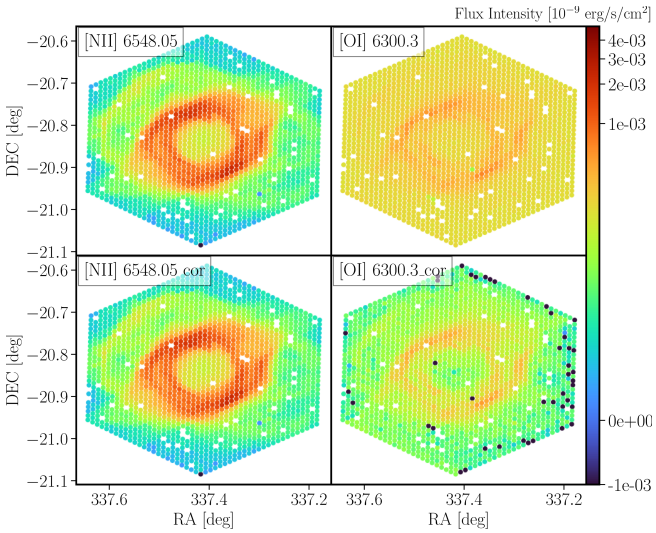

Figure 10. Comparison between the spatial distribution of the flux intensities for the [N II]6548 (left panels) and [O I]6300 (right panels) emission lines before (top panels) and after (bottom panels) applying the 2nd order sky correction. While the correction has no effect in e [N II]6548, it produces a clear improvement for [O I]6300.

into a single `astropy` Table, how to plot the spatial distribution of any of the delivered parameters, how to compare between different procedures adopted to deliver the same parameter or/and how to handle the RSP PDF are all included as comments within the code.

C. DATA DISTRIBUTION

Along this study we made use of the reduced LVM observation on the Helix nebula distributed as part of the SDSS-V DR19 [13]. As a result of the analysis performed by the LVM-DAP we distribute the following dataproducts:

- DAP file comprising the main results of the analysis as described in § 3 and Sánchez et al. (2025): https://ifs.astroscu.unam.mx/LVM_DR19_Helix/Helix_DR19_new.dap.fits.gz
- Spatial distribution of the flux intensities once applied the 2nd order sky subtraction described in § 3.1: https://ifs.astroscu.unam.mx/LVM_DR19_Helix/Helix_DR19_cor.fits.gz

D. FACILITIES

This study made use of the LVM facility, an infrastructure composed of four telescopes connected to three spectrographs installed at the Las Campanas Observatory, operated by the SDSS-V collaboration.

[13] https://dr19.sdss.org/sas/dr19/spectro/lvm/redux/1.1.1/0011XX/11111/60191/lvmSFrame-00004297.fits

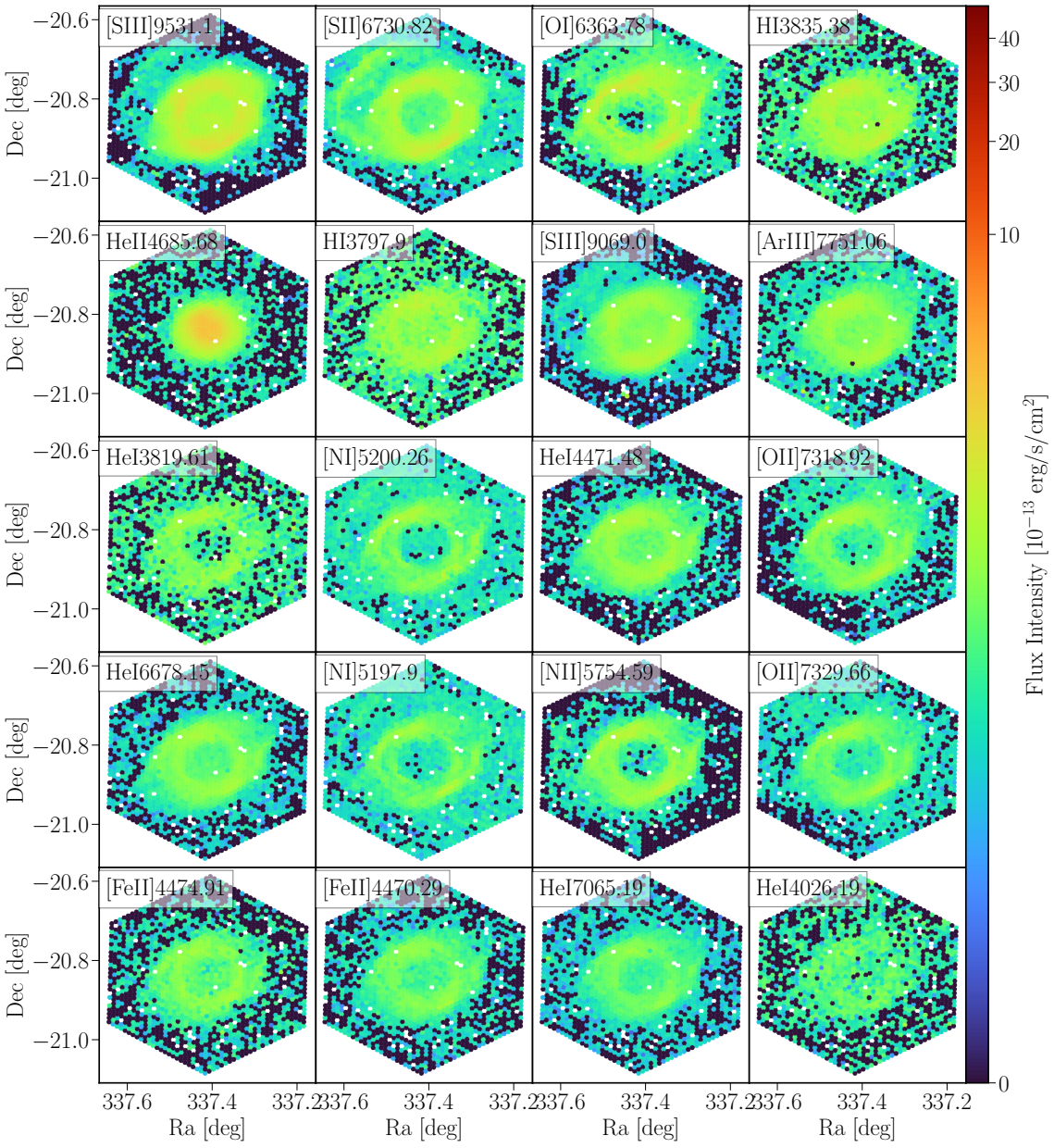

Figure 11. Similar figure as Fig. 4, for the subsequent 20 emission lines, ordered by integrated flux intensity.

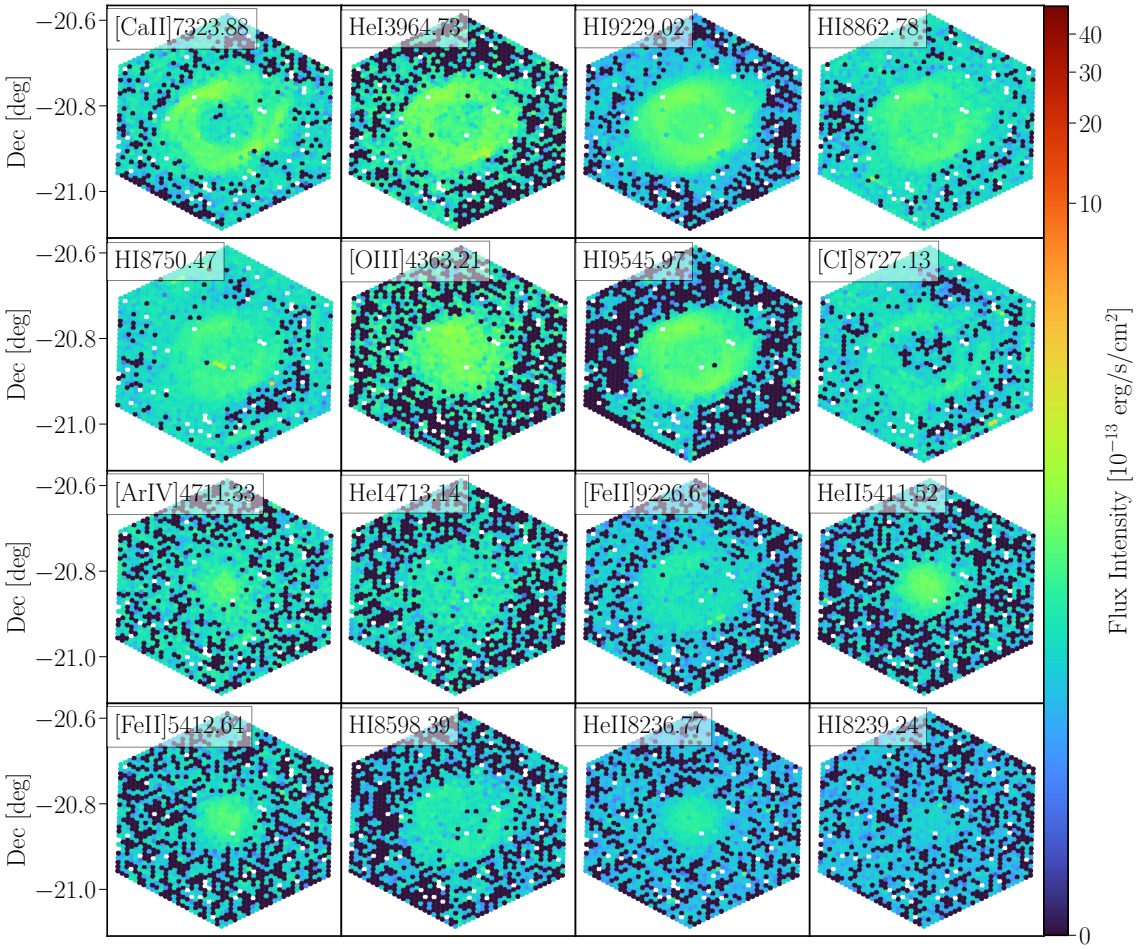

Figure 12. Similar figure as Fig. 4 and 11, for the subsequent 20 emission lines, ordered by integrated flux intensity.

REFERENCES

Andriantsaralaza, M., Zijlstra, A., & Avison, A. 2020, MNRAS, 491, 758, doi: 10.1093/mnras/stz3026

Benjamin, R. A., Skillman, E. D., & Smits, D. P. 1999, ApJ, 514, 307, doi: 10.1086/306923

Bruzual, G., & Charlot, S. 2003, MNRAS, 344, 1000, doi: 10.1046/j.1365-8711.2003.06897.x

Bublitz, J., Kastner, J. H., Hily-Blant, P., et al. 2022, A&A, 659, A197, doi: 10.1051/0004-6361/202141778

Cappellari, M., & Emsellem, E. 2004, PASP, 116, 138, doi: 10.1086/381875

Cerviño, M., Román-Zúñiga, C., Bayo, A., et al. 2013, A&A, 553, A32, doi: 10.1051/0004-6361/201220937

Cid Fernandes, R., Mateus, A., Sodré, L., Stasinska, G., & Gomes, J. M. 2011, STARLIGHT: Spectral Synthesis Code, Astrophysics Source Code Library. http://ascl.net/1108.006

Colombo, D., Kalinova, V., Bazzi, Z., et al. 2025, A&A, 699, A366, doi: 10.1051/0004-6361/202453179

Conroy, C. 2013, ARA&A, 51, 393, doi: 10.1146/annurev-astro-082812-141017

Drory, N., Blanc, G. A., Kreckel, K., et al. 2024, AJ, 168, 198, doi: 10.3847/1538-3881/ad6de9

Estrada-Dorado, S., Guerrero, M. A., Toalá, J. A., et al. 2025, MNRAS, 536, 2477, doi: 10.1093/mnras/stae2733

Etxaluze, M., Cernicharo, J., Goicoechea, J. R., et al. 2014, A&A, 566, A78, doi: 10.1051/0004-6361/201322941

Fernique, P., Allen, M. G., Boch, T., et al. 2015, A&A, 578, A114, doi: 10.1051/0004-6361/201526075

González-Torà, G., Sander, A. A. C., Egorova, E., et al. 2025, arXiv e-prints, arXiv:2509.04569, doi: 10.48550/arXiv.2509.04569

Gruenwald, R. B., & Viegas, S. M. 1992, ApJS, 78, 153, doi: 10.1086/191623

Harris, H. C., Dahn, C. C., Canzian, B., et al. 2007, AJ, 133, 631, doi: 10.1086/510348

Hawley, S. A. 1978, PASP, 90, 370, doi: 10.1086/130342

Henry, R. B. C., Kwitter, K. B., & Dufour, R. J. 1999, ApJ, 517, 782, doi: 10.1086/307215

Herbst, T. M., Bizenberger, P., Blanc, G. A., et al. 2024, AJ, 168, 267, doi: 10.3847/1538-3881/ad7948

Hilder, T., Casey, A. R., Dalcanton, J. J., et al. 2025, arXiv e-prints, arXiv:2510.07395, doi: 10.48550/arXiv.2510.07395

Husemann, B., Jahnke, K., Sánchez, S. F., et al. 2013, A&A, 549, A87, doi: 10.1051/0004-6361/201220582

Iskandarli, L., Farihi, J., Lothringer, J. D., et al. 2024, MNRAS, 534, 3498, doi: 10.1093/mnras/stae2286

Kingsburgh, R. L., & Barlow, M. J. 1994, MNRAS, 271, 257, doi: 10.1093/mnras/271.2.257

Kollmeier, J. A., Rix, H.-W., Aerts, C., et al. 2025, arXiv e-prints, arXiv:2507.06989, doi: 10.48550/arXiv.2507.06989

Kreckel, K., Egorov, O. V., Egorova, E., et al. 2024, A&A, 689, A352, doi: 10.1051/0004-6361/202449943

Lacerda, E. A. D., Sánchez, S. F., Mejía-Narváez, A., et al. 2022, arXiv e-prints, arXiv:2202.08027. https://arxiv.org/abs/2202.08027

Leene, A., & Pottasch, S. R. 1987, A&A, 173, 145

Leroy, A. K., Schinnerer, E., Hughes, A., et al. 2021, ApJS, 257, 43, doi: 10.3847/1538-4365/ac17f3

Meaburn, J., Boumis, P., López, J. A., et al. 2005, MNRAS, 360, 963, doi: 10.1111/j.1365-2966.2005.09083.x

Meaburn, J., López, J. A., & Richer, M. G. 2008, MNRAS, 384, 497, doi: 10.1111/j.1365-2966.2007.12710.x

Meaburn, J., Walsh, J. R., Clegg, R. E. S., et al. 1992, MNRAS, 255, 177, doi: 10.1093/mnras/255.2.177

Mejia-Narvaez, A., Bruzual, G., Sanchez, S. F., et al. 2021, arXiv e-prints, arXiv:2108.01697. https://arxiv.org/abs/2108.01697

Mellema, G. 1995, MNRAS, 277, 173, doi: 10.1093/mnras/277.1.173

O'Dell, C. R. 1962, ApJ, 135, 371, doi: 10.1086/147277

—. 1998, AJ, 116, 1346, doi: 10.1086/300506

—. 2005, RMxAC, 23, 5, doi: 10.48550/arXiv.astro-ph/0505539

O'Dell, C. R., Henney, W. J., & Ferland, G. J. 2007, AJ, 133, 2343, doi: 10.1086/513011

O'Dell, C. R., McCullough, P. R., & Meixner, M. 2004, AJ, 128, 2339, doi: 10.1086/424621

Osterbrock, D. E., & Ferland, G. J. 2006, Astrophysics of gaseous nebulae and active galactic nuclei, 2nd. ed., (Sausalito, CA: University Science Books)

Peimbert, M., Peimbert, A., & Luridiana, V. 2017, RMxAC, 49, 181

Peimbert, M., & Torres-Peimbert, S. 1983, in IAU Symposium, Vol. 103, Planetary Nebulae, ed. L. H. Aller, 233–242

Sánchez, S. F. 2006, AN, 327, 850, doi: 10.1002/asna.200610643

Sánchez, S. F., Pérez, E., Sánchez-Blázquez, P., et al. 2016, RMxAA, 52, 21. https://arxiv.org/abs/1509.08552

Sánchez, S. F., Mejía-Narváez, A., Egorov, O. V., et al. 2025, AJ, 169, 52, doi: 10.3847/1538-3881/ad93bb

Sarbadhicary, S. K., Long, K. S., Raymond, J. C., et al. 2025, arXiv e-prints, arXiv:2507.08257, doi: 10.48550/arXiv.2507.08257

Sattler, N., Méndez-Delgado, J. E., Kreckel, K., et al. 2025, arXiv e-prints, arXiv:2512.02802, doi: 10.48550/arXiv.2512.02802

Schönberner, D., Jacob, R., Steffen, M., et al. 2005, A&A, 431, 963, doi: 10.1051/0004-6361:20041669

SDSS Collaboration, Adamane Pallathadka, G., Aghakhanloo, M., et al. 2025, arXiv e-prints, arXiv:2507.07093, doi: 10.48550/arXiv.2507.07093

Tylenda, R., Siódmiak, N., Górny, S. K., Corradi, R. L. M., & Schwarz, H. E. 2003, A&A, 405, 627, doi: 10.1051/0004-6361:20030645

Villa-Durango, M. A., Barrera-Ballesteros, J., Román-Zúñiga, C. G., et al. 2025, MNRAS, 543, 1196, doi: 10.1093/mnras/staf1530

Walsh, J. R., & Meaburn, J. 1987, MNRAS, 224, 885, doi: 10.1093/mnras/224.4.885

Warner, J. W., & Rubin, V. C. 1975, ApJ, 198, 593, doi: 10.1086/153638

Wright, E. L., Eisenhardt, P. R. M., Mainzer, A. K., et al. 2010, AJ, 140, 1868, doi: 10.1088/0004-6256/140/6/1868

Yan, R., Chen, Y., Lazarz, D., et al. 2019, ApJ, 883, 175, doi: 10.3847/1538-4357/ab3ebc

Academic Affiliations

[3]*Universidad Nacional Autónoma de México, Instituto de Astronomía, AP70-264, CDMX 04510, México.*
[4]*Departamento de Astronomía, Universidad de Chile, Camino del Observatorio 1515, Las Condes, Santiago, Chile.*
[5]*Astronomisches Rechen-Institut, Zentrum für Astronomie der Universität Heidelberg, Mönchhofstraße 12-14, D-69120 Heidelberg, Germany.*
[6]*Universidad Nacional Autónoma de México, Inst. de Ciencias Físicas, Av. Universidad S/N, Chamilpa, 62200 Cuernavaca, Morelos, México.*
[7]*McDonald Observatory, The University of Texas at Austin, 1 University Station, Austin, TX 78712-0259, USA.*
[8]*Observatories of the Carnegie Institution for Science, 813 Santa Barbara Street, Pasadena, CA 91101, USA.*
[9]*Instituto de Estudios Astrofísicos, Facultad de Ingeniería y Ciencias, Universidad Diego Portales, Av. Ejército Libertador 441, Santiago, Chile.*
[10]*New York University Abu Dhabi, PO Box 129188, Abu Dhabi, UAE.*
[11]*Center for Astrophysics and Space Science (CASS), New York University Abu Dhabi, PO Box 129188, Abu Dhabi, UAE.*
[12]*Sternberg Astronomical Institute, Lomonosov Moscow State University, Universitetskij pr., 13, Moscow, 119234, Russia.*
[13]*Department of Astronomy, Universidad de LaSerena, Av. Raul Bitran 1302, La Serena, Chile.*
[14]*Max-Planck-Institut für Astronomie, Königstuhl 17, D-69117, Heidelberg, Germany.*
[15]*Universidad Católica del Norte, Núcleo UCN en Arqueología Galáctica-Inst. de Astronomía, Av. Angamos 0610, Antofagasta, Chile.*
[16]*Universidad Católica del Norte, Departamento de Ingeniería de Sistemas y Computación, Av. Angamos 0610, Antofagasta, Chile.*
[17]*Chinese Academy of Sciences South America Center for Astronomy, National Astronomical Observatories, CAS, Beijing 100101, China.*
[18]*Instituto de Astronomía, Universidad Católica del Norte, Av. Angamos 0610, Antofagasta, Chile.*
[19]*Center for Astrophysics and Space Astronomy, University of Colorado, 389 UCB, Boulder, CO 80309-0389, USA.*
[20]*Instituto de Radioastronomía y Astrofísica, Universidad Nacional Autónoma de México, Morelia 58089, Michoacán, México; Facultad de Ciencias de la Tierra y el Espacio, Universidad Autónoma de Sinaloa, Josefa Ortiz de Domínguez S/N, Culiacán 80040, Sin., México.*
[21]*Space Telescope Science Institute, 3700 San Martin Drive, Baltimore, MD 21218, USA.*
[†]*This project is part of the SDSS collaboration.*